

# GAS GEOCHEMISTRY AT GRANDE COMORE AND MAYOTTE VOLCANIC ISLANDS (COMOROS ARCHIPELAGO), INDIAN OCEAN

Marco Liuzzo<sup>1</sup>, Andrea Di Muro<sup>2</sup>, Andrea Luca Rizzo<sup>3</sup>, Antonio Caracausi<sup>3</sup>, Fausto Grassa<sup>3</sup>, Nicolas Fournier<sup>4</sup>, Bafakih Shafik<sup>5</sup>, Guillaume BOUDOIRE<sup>6</sup>, Massimo Coltorti<sup>7</sup>, Manuel Moreira<sup>8</sup>, and Francesco Italiano<sup>9</sup>

<sup>1</sup>Istituto Nazionale di Geofisica e Vulcanologia - Sezione di Palermo

<sup>2</sup>Institut De Physique Du Globe De Paris

<sup>3</sup>Istituto Nazionale di Geofisica e Vulcanologia

<sup>4</sup>GNS Science

<sup>5</sup>Observatoire Volcanologique du Karthala - CNDRS, Comoroes

<sup>6</sup>Laboratoire Magmas et Volcans, UCA, CNRS, IRD, OPGC

<sup>7</sup>Earth Science Department, University of Ferrara

<sup>8</sup>ISTO, Institut de Sciences de la Terre d'Orléans, France

<sup>9</sup>INGV

November 22, 2022

## Abstract

The Comoros Archipelago is an active geodynamic region of intra-plate volcanism within which the youngest and oldest islands (Grande Comore and Mayotte respectively) are characterized by recent volcanic activity. The frequent eruptions of the large shield volcano Karthala on Grande Comore (last eruption 2007), and the recent birth of a large submarine volcano since 2018 at the submarine base of Mayotte are associated with permanent fumarolic emissions, bubbling gas seeps, and soil gas emissions, which are studied in detail here for the first time. CO<sub>2</sub> fluxes and chemical and isotopic gas compositions acquired during two surveys in 2017 and 2020 are integrated with older datasets collected between 2005 and 2016, permitting the identification of a possible influence of the recent volcanic and magmatic activity at Mayotte. At Karthala, high gas fluxes with high temperature, and a marked magmatic signature are concentrated close to the summit crater area, while only weaker emissions with a stronger biogenic signature are found on the volcano flanks. At Mayotte, lower temperature and higher CH<sub>4</sub> content are recorded in two main seep areas of CO<sub>2</sub>-rich fluid bubbling, while soil emissions on land record a higher proportion of magmatic fluids compared to Karthala. Our preliminary results reveal two quite separate gas emission patterns for each island that are distinct in composition and isotopic signatures, and well-correlated with the present state of volcanic activity. This work may potentially provide support for local observation infrastructures and contribute to the improvement in volcanic and environmental monitoring

1 TITLE

2 GAS GEOCHEMISTRY AT GRANDE COMORE AND MAYOTTE VOLCANIC ISLANDS (COMOROS  
3 ARCHIPELAGO), INDIAN OCEAN

4  
5 **Marco Liuzzo**<sup>(1,7)</sup>, Andrea Di Muro<sup>(2,3)</sup>, Andrea Luca Rizzo<sup>(1)</sup>, Antonio Caracausi<sup>(1)</sup>, Fausto Grassa<sup>(1)</sup>,  
6 Nicolas Fournier<sup>(4)</sup>, Bafakih Shafik<sup>(5)</sup>, Guillaume Boudoire<sup>(1,6)</sup>, Massimo Coltorti<sup>(7)</sup>, Manuel  
7 Moreira<sup>(8)</sup>, Francesco Italiano<sup>(1)</sup>

8 <sup>(1)</sup> Istituto Nazionale di Geofisica e Vulcanologia, Sezione di Palermo – Italy,  
9 <sup>(2)</sup> Université de Paris, Institut de physique du globe de Paris, CNRS, F-75005 Paris, France  
10 <sup>(3)</sup> Observatoire volcanologique du Piton de la Fournaise, Institut de physique du globe de Paris,  
11 F-97418 La Plaine des Cafres, France  
12 <sup>(4)</sup> GNS Science, New Zealand,  
13 <sup>(5)</sup> Observatoire Volcanologique du Karthala - CNDRS, Comoroès,  
14 <sup>(6)</sup> Université Clermont Auvergne, CNRS, IRD, OPGC, Laboratoire Magmas et Volcans, F-63000  
15 Clermont-Ferrand, France,  
16 <sup>(7)</sup> Università di Ferrara, Dipartimento di Fisica e Scienze della Terra – Italy,  
17 <sup>(8)</sup> ISTO, Institut de Sciences de la Terre d' Orléans, France  
18

19 Corresponding author: Marco Liuzzo (marco.liuzzo@ingv.it)

20 **Key Points:**

- 21 • Map of the spatial distribution of ground CO<sub>2</sub> emissions and its isotopic characteristics in  
22 both islands Grande Comore and Mayotte  
23 • Geochemical characterisation of fumarolic and hydrothermal gases in terms of both  
24 primary component species and isotopic characteristics  
25 • Correlation between the variability of geochemical tracers and the new submarine volcano  
26 off Mayotte and its implications for the risk to the island's inhabitants

27 **Abstract**

28 The Comoros Archipelago is an active geodynamic region of intra-plate volcanism within which the  
29 youngest and oldest islands (Grande Comore and Mayotte respectively) are characterized by  
30 recent volcanic activity. The frequent eruptions of the large shield volcano Karthala on Grande  
31 Comore (last eruption 2007), and the recent birth of a large submarine volcano since 2018 at the  
32 submarine base of Mayotte are associated with permanent fumarolic emissions, bubbling gas  
33 seeps, and soil gas emissions, which are studied in detail here for the first time. CO<sub>2</sub> fluxes and  
34 chemical and isotopic gas compositions acquired during two surveys in 2017 and 2020 are

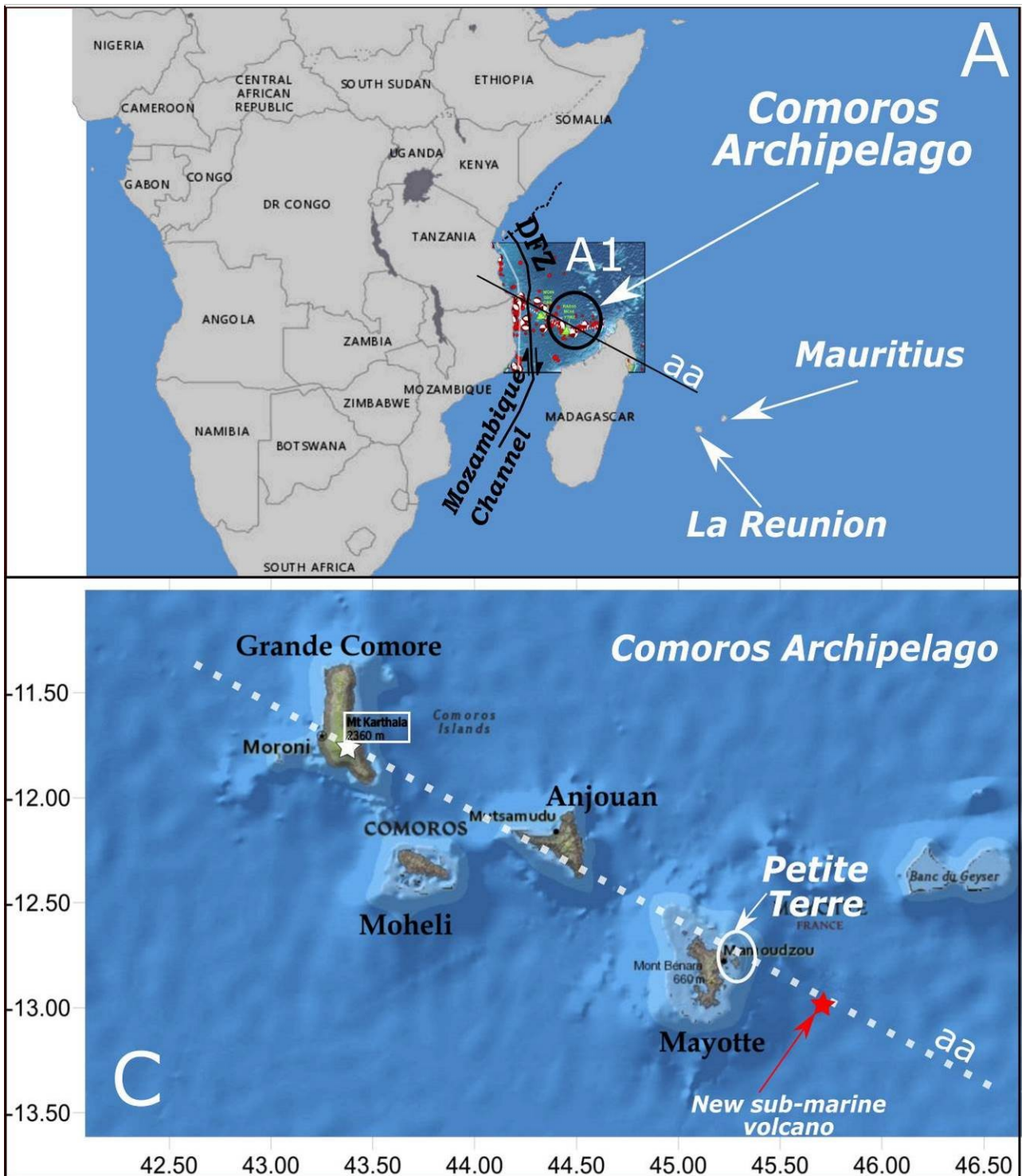
35 integrated with older datasets collected between 2005 and 2016, permitting the identification of a  
36 possible influence of the recent volcanic and magmatic activity at Mayotte.

37 At Karthala, high gas fluxes with high temperature, and a marked magmatic signature are  
38 concentrated close to the summit crater area, while only weaker emissions with a stronger  
39 biogenic signature are found on the volcano flanks. At Mayotte, lower temperature and higher  
40 CH<sub>4</sub> content are recorded in two main seep areas of CO<sub>2</sub>-rich fluid bubbling, while soil emissions on  
41 land record a higher proportion of magmatic fluids compared to Karthala. Our preliminary results  
42 reveal two quite separate gas emission patterns for each island that are distinct in composition  
43 and isotopic signatures, and well-correlated with the present state of volcanic activity. This work  
44 may potentially provide support for local observation infrastructures and contribute to the  
45 improvement in volcanic and environmental monitoring.

## 46 1. Introduction

47 Comoros archipelago is located in the Mozambique Channel between the east coast of Africa and  
48 the north-western coast of Madagascar. The formation of a huge submarine volcanic edifice since  
49 2018, about 50 km offshore east of Mayotte, has prompted a renewal of multidisciplinary  
50 researches on the seismo-volcanic activity of the Comoros Archipelago by the international  
51 volcanological community (Bachèlery et al., 2019; Berthod et al., 2020; Cesca et al., 2020; Feuillet  
52 et al., 2019; Lemoine et al., 2020; REVOSIMA, 2019). The archipelago consists of four main islands  
53 from NW to SE: Grande Comore, Mohéli, Anjouan, and Mayotte (Figure 1), amongst which Grande  
54 Comore hosts the large and frequently active basaltic Karthala volcano (last eruption in 2007).  
55 Subaerial Holocene volcanic activity related to a range of alkaline magma compositions (from  
56 basanite to phonolite) has been documented in the other islands (Bachèlery et al., 2016; Michon  
57 et al., 2016; Tzevahirtzian et al., 2021 and references therein). Comoros Archipelago is considered  
58 as the potential diffuse Lwandle-Somali sub-plate boundary and part of the SE extension of the  
59 East African Rift System (Michon et al., 2016; Famin et al., 2020). The recent review of  
60 morphological, geological and chronological data of Tzevahirtzian et al. (2021) suggests that  
61 Mayotte and Moheli are the oldest islands, while Anjouan and Grande Comore are the most  
62 recent ones. The recent volcanism of Karthala in Grande Comore has been interpreted as hot-spot-  
63 related by geochemical studies (e.g. Class et al., 1998). Grande Comore and Anjouan are high  
64 altitude volcanic islands, intersected by well developed triple-armed volcanic rifts. On the  
65 contrary, Moheli and Mayotte are lower islands, with less well developed rift zones, and a wide  
66 insular shelf, which is very narrow on Grande Comore and Anjouan. Karthala is the second most

67 active volcano in the Indian Ocean, after Piton de la Fournaise in La Réunion island, with  
68 permanent hydrothermal and fumarolic emissions close to its summit area (Bachelery et al., 1996;  
69 Bernabeu et al., 2018). Two years after the last summit Karthala eruption, Bernabeu et al. (2018)  
70 document high CO<sub>2</sub> fluxes in the soil close to the eruptive vent. However, the absence of chemical  
71 or isotopic analysis did not permit to attribute these emissions to the recently emplaced magma or  
72 to deeper sources. Seep areas of low-temperature CO<sub>2</sub>-rich bubbling gases have been reported for  
73 the first time between 1993 and 1998 at Mayotte, on the small island (Petite Terre) located on its  
74 eastern side (Traineau et al., 2006 and references therein).



75

76 Figure 1. Map of the Comoros Archipelago, which is located on the northern zone of the Mozambique Channel (A), in  
 77 which is also shown the Davie Fracture zone (DZF). The elongated trend N120° "a-a" of the islands corresponding with  
 78 the recognised regional structural trend well defined by distribution of the 1901–2018 seismicity for  $M > 4$  showed in  
 79 the inset A1 (from Lemoine et al., 2020 modified). In (B) highlighted on the map is the little island on the east coast of  
 80 Mayotte called Petite Terre, where have been acquired all the measurements (both from the soil and from the  
 81 bubbling area on the sea) mentioned in this paper regarding Mayotte island. The white star at Grande Comore  
 82 indicates the Karthala volcano. The red star is the approximate location of the new submarine volcano.

83 In this work, we focus on the gaseous emissions on the oldest (Mayotte) and youngest (Grande  
 84 Comore) islands, which are also the two recently active volcanic systems of the Comoros

85 archipelago, with the aim at constraining the extent and spatial distribution of the outgassing  
86 areas and the geochemical signature of the gas emissions. Data were collected by a team of  
87 researchers from IPGP/OVPF and INGV who carried out surveys on the two islands between 2017  
88 and 2019. In addition, we included data from older measurement campaigns which were  
89 undertaken for different purposes between 2005 and 2014. The results of the geochemical  
90 investigation highlight the differences in outgassing characteristics between the two volcanic  
91 islands and their link with the recent volcanic activity. We perform a comparison with the gas  
92 geochemistry of La Réunion island, where a deep and plume-like undegassed mantle contribution  
93 has been since long identified.

94 Grande Comore and Mayotte are densely populated islands and in view of the high level of seismic  
95 and volcanic activity and the related hazards, these first results represent a significant contribution  
96 to pave the way for future activities on geochemical monitoring and hazard mitigation.

97

## 98 2. Geological context

99 The islands of the Comorian archipelago are located within the Mozambique Channel in a  
100 particularly complex geodynamic region where the tectonic features are yet to be unambiguously  
101 defined. The main and better known tectonic structure, the Davie Fracture Zone (DFZ) (Phethean  
102 et al., 2016), is considered the kinematic hinge that allowed the southward drift of Madagascar  
103 following the Gondwana breakup. Despite its well defined structure, the DFZ has been described  
104 as either a western transform fault (Coffin et al., 1986) or as a continent-ocean transform margin  
105 (Gaina et al., 2013) of the Western Somali Basin (Figure 1A). The alignment of the islands is NW-SE  
106 and coincident with the main seismic zone of the archipelago (Figure 1 B - from Lemoine et al.,  
107 2020, modified). This orientation of islands separates the North Somali basin, which is agreed to  
108 be oceanic, and the South Somali basin, which for some authors is thought to be oceanic crust  
109 (e.g. Klimke et al., 2016; Rabinowitz et al., 1983), while other authors identify this as a thinned  
110 continental crust (e.g. Bassias & Leclaire, 1990; Roach et al., 2017).

111 The two main hypotheses that have been developed over time to explain the origin of the  
112 Comoros volcanism are:

- 113 a) a mantle plume, which interacts with the oceanic lithosphere (Claude-Ivanaj et al., 1998;  
114 Class et al., 2005; Deniel, 1998; Nougier et al., 1986; Emerick and Duncan, 1982; Hajash and

115 Armstrong, 1972). The link with a deep mantle hot spot has been invoked to explain the  
116 eastward migration of volcanism age, but also to explain the variability of geochemical  
117 magma composition measured along the Archipelago. Karthala lavas are those recording a  
118 stronger hot spot signature (Bachèlery and Hémond, 2016; Claude-Ivanaj et al., 1998; Class  
119 et al., 2009; Coltorti et al., 1999). Recent seismic tomography (French and Romanowicz,  
120 2015) fails to unambiguously identify a deep plume rooted in the mantle below Comoros  
121 archipelago.

122 b) the reactivation of regional lithospheric structures, which interact with asthenospheric  
123 processes. This hypothesis rejects the previous model because it is inconsistent with the  
124 current volcanic activity which includes both Karthala volcano and the recent and still  
125 ongoing submarine volcanic activity eastward of Mayotte and with the absence of a clear  
126 age decrease along the archipelago (Tzevahirtzian et al., 2021; Famin et al., 2020; Lemoine  
127 et al., 2020; Michon, 2016; Nougier et al., 1986)

128 At Mayotte, the volcanic activity becomes increasingly older from the eastern side (Petite Terre  
129 island), to the western main island (Grande Terre) (Nehlig et al., 2013). The still ongoing (at the  
130 time of writing), large-volume and long-lasting sub-marine eruption of Mayotte, the largest  
131 submarine event ever detected by monitoring networks (Cesca et al., 2020; Lemoine et al., 2020),  
132 challenges current models on the origin of Comoros volcanism. Since 2018, several km<sup>3</sup> of evolved  
133 basanite lava have been emitted on the 3.5 km deep seafloor 50 km east from Mayotte from a  
134 deep source located in the upper lithospheric mantle (Bachèlery et al., 2019; Berthod et al., 2020;  
135 Lemoine et al. 2020). The new volcano grows on a N120° oriented volcanic ridge, which runs along  
136 the eastern submarine flank of Mayotte and whose western subaerial tip is the small island of  
137 Petite Terre (Tzevahirtzian et al., 2021; Figure 1C). On Petite Terre, recent volcanic activity has  
138 built on the coral reef a set of Holocene basaltic scoria cones and phonolitic maars (Zinke et al.,  
139 2001; Nehlig et al., 2013), and two main areas of low-temperature CO<sub>2</sub>-rich gas bubbling seeps. A  
140 first bubbling area occurs in the NE part of Petite Terre inside the intracrateric lake of the Dziani  
141 phonolitic maar, where several CO<sub>2</sub>- and CH<sub>4</sub>- rich bubbling spots have been identified (Milesi et  
142 al., 2020). A second area, first described in 1998 on the eastern tidal flat of Petite Terre is located  
143 close to the “Airport beach” (BAS site; Traineau, 2006; Sanjuan, 2008). There, tens of bubbling  
144 spots occur at the southern feet of the large “Vigie” phonolitic maar, on a muddy flat area exposed  
145 to significant tide and extended for about 250x300m from the beach (see also Figure 8A-8C).

146 In Grande Comore, at least three volcanic massifs have been identified: the old and inactive  
147 M'Badjini massif in the southernmost part of Grande Comore, the rarely active La Grille volcano in  
148 the north (last dated eruption: 1029-1424 CE) and in between the frequently active Karthala shield  
149 volcano (last eruption: 2007) (Bachelery et al., 2016 and references therein). Karthala volcano is a  
150 large (summit elevation 2361 m) basaltic shield volcano, the highest relief of the Comoros  
151 Archipelago, and exhibits well-developed rift zones diverging from a 3.6 x 2.7 km wide summit  
152 polylobate caldera. The average frequency of its eruptions, occurring both at the volcano summit  
153 and on the flanks, is of one eruption every 6-8 years over the past 100 years and the volcano was  
154 frequently active in the 1991-2007 period (Bachèlery et al., 2016). The self-potential study of the  
155 summit caldera performed by Lénat et al. (1998) and Bernabeu et al. (2018) show that the main  
156 hydrothermal activity of the volcano does not occur below the main summit crater (Choungou-  
157 Chahalé), but on the northern part of the summit caldera, where several recent eruptions have  
158 occurred. We sampled two main areas, the first one correspond to steaming grounds and  
159 fumaroles located close to the Choungou-Chagnoumeni pit crater located in the northern part of  
160 the caldera and filled by the lavas of the last eruption in 2007 (see Figure 7B site CC) and a second  
161 one, the "Soufrière" fumarolic area located on recent lavas 1.7 km north of the summit caldera,  
162 along the northern rift zone (see Figure 7B site LS).

163

### 164 3. Materials and Methods

#### 165 3.1 Previous datasets

166 In this study, we present the results of our 2017-2020 surveys on soil gas fluxes and their  
167 composition as well as on the composition of Mayotte gas bubbling and Grande Comore fumarolic  
168 areas (Figures 7 and 8). Our dataset is integrated with older and partly unpublished surveys  
169 acquired on the two islands.

170 At Mayotte, the BAS bubbling site has been first studied by BRGM in November 2005 (Traineau,  
171 2006; BRGM report) and April 2008 (Sanjouan, 2008; BRGM report) in terms of spatial distribution,  
172 gas fluxes, temperature, pH and chemical and isotopic composition. In the BRGM campaigns,  $\delta^{13}\text{C}$   
173 and dD data were not acquired on methane and preliminary noble gases data were produced by  
174 the IPGP laboratory (M. Moreira). A rich biological, chemical and isotopic dataset (C-H-S species,  
175 not including the noble gases) of the Dziani intracrateric lake and of its bubbling was acquired in  
176 the period 2012-2018 (Jovovic et al., 2017; Leboulanger et al., 2017; Gérard et al., 2018; Hugoni et

177 al., 2018; Milesi et al., 2019; 2020; Cadeau et al., 2020). Milesi et al. (2020) collected fluids in  
178 August 2016 by focusing on the spatial distribution and C-H chemical and isotopic composition of  
179 bubbling gases in the Dziani lake, while only a single analysis (G7 sample) is reported for the BAS  
180 area.

181 On Karthala volcano, the summit steaming grounds and fumarole have been first described (but  
182 not sampled) by Bachelery and Coudray (1993). Soil CO<sub>2</sub> and temperature profiles were measured  
183 between March 2008 and January 2010 in the hot grounds (40-80°C) close to the summit 2007 pit  
184 crater by Bernabeu et al. (2018). The first detailed study of the gas emissions in Grande Comore  
185 was performed in 2014 in the frame of an international geothermal exploration project  
186 (Benavente et al., 2015; Chaheire et al., 2016).

187

### 188 3.2 Gas sampling and analysis

189 Grande Comore field works were performed in December 2017 (volcano flanks) and October 2018  
190 (volcano flanks and summit area). Mayotte surveys were carried out on Petite Terre (Figure 1) in  
191 four campaigns, i.e. in December 2018, April 2019, September 2019 and November 2020 (Table 1).

192 Soil gas samples for isotopic ( $\delta^{13}\text{C}$  in CO<sub>2</sub>) and chemistry analysis were collected by introducing a  
193 steel probe into the ground (50 cm long) and collected in 10 mL Exetainer glass vials and in two-  
194 stopcock glass bottles 100mL.

195 Dry gases from fumarolic fields at Karthala were collected using a steel probe (the same as for soil  
196 sampling) introduced into the ground and connected to a three-way valve equipped of a syringe  
197 and a tube connected to the bottles for gas storage. Bubbling gases at Mayotte have been taken  
198 using a steel funnel connected to a three-way valve equipped of a syringe and a tube connected to  
199 two-stopcock glass bottles 250mL (chemistry and C-H isotopic analysis), two-stopcock steel bottles  
200 100mL (noble gases elemental and isotopic analysis), and pre-weighed evacuated bottles  
201 containing absorbing alkaline solution (4N NaOH) following the method of Giggenbach and Goguel  
202 (1989).

203 All the gas samples were analysed at the laboratories of INGV (Istituto Nazionale di Geofisica e  
204 Vulcanologia), Sezione di Palermo, for their chemistry and for the isotopic compositions of noble  
205 gases (He, Ne, and Ar), C of CO<sub>2</sub>, and C and H of CH<sub>4</sub>. Analyses are reported in Table 3. The chemical  
206 composition of He, H<sub>2</sub>, O<sub>2</sub>, N<sub>2</sub>, CO, CH<sub>4</sub>, and CO<sub>2</sub> was measured by a gas chromatograph (Clarus 500,

207 Perkin Elmer) equipped with a 3.5-m column (Carboxen 1000) and double detector (hot-wire  
208 detector and flame ionization detector [FID]), for which the analytical errors were < 3%.

209 The C-isotope composition of CO<sub>2</sub> (expressed as δ<sup>13</sup>C ‰) vs. V-PDB (Vienna-Pee Dee Belemnite)  
210 was determined using a continuous-flow isotope-ratio mass spectrometer (Thermo Delta Plus XP,  
211 Finnigan), connected to a gas chromatograph (Trace GC) and interface (Thermo GC/C III, Finnigan).  
212 The gas chromatograph and its column (length = 30 m and i.d. = 0.32 mm; Poraplot-Q) were  
213 operated at a constant temperature of 50°C using He as the carrier gas. The analytical errors were  
214 <0.1‰. The same instrument has been used for C and H isotope determination in CH<sub>4</sub>, where a  
215 combustion interface (Thermo GC III, Finnigan) was used to produce CO<sub>2</sub> from CH<sub>4</sub> and a gas-  
216 chromatograph/thermal-conversion interface provided online high-temperature conversion of CH<sub>4</sub>  
217 into H. The SDs for the δ<sup>13</sup>C and δD measurements of CH<sub>4</sub> were <0.2 and <2.5‰, respectively.

218 Noble gas (He, Ne, Ar) isotopes were analyzed at the noble-gas laboratory at INGV-Palermo. <sup>3</sup>He  
219 and <sup>4</sup>He were measured into a split flight tube mass spectrometer (GVI-Helix SFT), after  
220 purification of the sample from the major gaseous species and separation from the other noble  
221 gases. <sup>20</sup>Ne was determined by admitting Ne into a multicollector mass spectrometer (Thermo-  
222 Helix MC plus), after purification procedure into a stainless steel ultra-high vacuum line distinct  
223 from that of He and Ar, as above described for helium. The <sup>3</sup>He/<sup>4</sup>He ratio is expressed as R/R<sub>a</sub>  
224 (being R<sub>a</sub> the He isotope ratio of air and equal to 1.39·10<sup>-6</sup>) with an analytical uncertainty (1σ)  
225 below 0.3%. Hereafter we discuss the <sup>3</sup>He/<sup>4</sup>He ratio corrected for atmospheric contamination  
226 using the measured <sup>4</sup>He/<sup>20</sup>Ne ratio (e.g., Sano and Wakita, 1985) that is reported in units of R<sub>c</sub>/R<sub>a</sub>,  
227 as follows:

$$228 \quad \frac{R}{R_a} = \frac{\left(\frac{R_m}{R_a}\right) \cdot \left(\frac{{}^4\text{He}}{{}^{20}\text{Ne}}\right)_m - \left(\frac{{}^4\text{He}}{{}^{20}\text{Ne}}\right)_a}{\left(\frac{{}^4\text{He}}{{}^{20}\text{Ne}}\right)_m - \left(\frac{{}^4\text{He}}{{}^{20}\text{Ne}}\right)_a} \quad (1)$$

229 where subscripts *m* and *a* refer to measured and atmosphere theoretical values, respectively [(He/  
230 Ne)<sub>a</sub> = 0.318] (Ozima and Podosek, 1983). We highlight that the correction on the <sup>3</sup>He/<sup>4</sup>He ratio is  
231 small or negligible for most of the gas samples [(<sup>4</sup>He/<sup>20</sup>Ne)<sub>m</sub> >> (<sup>4</sup>He/<sup>20</sup>Ne)<sub>a</sub>].

232 The Ar elemental and isotopic composition (<sup>36</sup>Ar, <sup>38</sup>Ar, and <sup>40</sup>Ar) were quantified in a multicollector  
233 mass spectrometer (Helix MC-GVI). The analytical uncertainty (1σ) for single <sup>40</sup>Ar/<sup>36</sup>Ar

234 measurements was <0.1%.  $^{40}\text{Ar}$  was corrected for air contamination ( $^{40}\text{Ar}^*$ ) in samples showing  
235  $^{40}\text{Ar}/^{36}\text{Ar}>315$  assuming that the  $^{36}\text{Ar}$  present derived from atmosphere, as follows:

236 
$$^{40}\text{Ar}^i = ^{40}\text{Ar}_{\text{sample}} - \text{Ar}_{\text{sample}} \cdot i \cdot i \quad (2)$$

237

238 Typical blanks for He, Ne, and Ar were  $<10^{-15}$ ,  $<10^{-16}$ , and  $<10^{-14}$  mol, respectively, and are at least  
239 two orders of magnitude lower than the sample signals at the relative mass spectrometers.  
240 Further details on samples purification and analysis are described by Rizzo et al. (2019) and  
241 Boudoire et al (2020).

### 242 3.3 Soil CO<sub>2</sub> fluxes

243 The soil CO<sub>2</sub> emissions data presented in this study have been acquired drawing on two different  
244 methods: accumulation chamber (Chiodini et al. 1998) and dynamic concentration (Gurrieri and  
245 Valenza, 1988). The methods differ owing to the fact that different teams carried out  
246 measurement surveys on different islands at different times. However, each single measurement  
247 campaign is consistent for the method used (Table 1).

#### 248 3.3.1 Accumulation chamber method

249 Both Benavente et al. (2015) surveys in Grande Comore and two of our surveys at Mayotte  
250 (September 2019 and November 2020) adopted the accumulation chamber method for  
251 measurements of soil CO<sub>2</sub> flux emissions using a West Systems portable accumulation chamber  
252 equipped with two different IR spectrometers. Benavente's campaign used a West System  
253 portable instrument with a LI-COR 820 IR and a 200 mm diameter chamber (West System chamber  
254 B), which introduces soil gas through the infrared spectrometer via tubing with an inline Mg(ClO<sub>4</sub>)<sub>2</sub>  
255 filter (avoiding the absorption of moisture which may cause interference in CO<sub>2</sub> concentration).  
256 Our campaigns in 2019 and 2020 at Mayotte Island used a West Systems portable accumulation  
257 chamber equipped with a Dräger Polytron IR sensor and a chamber with the same geometry as the  
258 one used by Benavente in Grande Comore (West system chamber B). We recorded soil  
259 temperature at each measurement location using a handheld Type K thermocouple probe inserted  
260 to 10 cm below ground level. In addition, pressure measurements and other weather parameters  
261 were recorded by a hand-held instrument meter (Kestrel 5000 series). Soil CO<sub>2</sub> flux ( $\text{g m}^{-2} \text{d}^{-1}$ ) from  
262 each site were calculated using the following equation (1):

263 
$$\text{CO}_2 = 44.01 \cdot \frac{86400 \cdot P}{10^6 \cdot R \cdot T_k} \cdot \frac{V}{A} \cdot \frac{\delta_c}{\delta_t} \quad (3)$$

264 where  $\delta_c/\delta_t$  is the change in the CO<sub>2</sub> concentration with time (ppm s<sup>-1</sup>), P is the measured pressure  
265 in mbar, R is the gas constant (bar L K<sup>-1</sup> mol<sup>-1</sup>), T is the measured temperature (K), V is the chamber  
266 net volume (0.006186 m<sup>3</sup>) and A is chamber inlet net area (0.0314 m<sup>2</sup>). The measurement accuracy  
267 of the CO<sub>2</sub> flux measurements method is ±12.5 % (Evans et al., 2001)

### 268 3.3.2 Dynamic concentration method

269 In our Grande Comore surveys, we focused on CO<sub>2</sub> soil emissions on the volcano flanks, where the  
270 Benavente et al. (2015) surveys failed in identifying significant anomalies using the accumulation  
271 chamber method. Therefore, we performed most of our measurements using the dynamic  
272 concentration method in our 2017 and 2018 field works and compared them with a subset  
273 acquired on the same sites using the accumulation chamber technique. This approach permits us  
274 to compare the Karthala dataset with that acquired on the Piton de la Fournaise volcano (Liuzzo et  
275 al., 2015). The dynamic concentration method (Gurrieri and Valenza, 1988) is based on an  
276 empirically identified relationship between soil CO<sub>2</sub> flux and CO<sub>2</sub> concentration in a gas mixture  
277 obtained by diluting soil gas with air (dynamic concentration), by means of a specific 50 cm probe  
278 inserted into the soil. Through a constant flux rate of 0.8 l/m, the gas from the soil is pumped to an  
279 IR spectrophotometer which measures CO<sub>2</sub> concentration. The spectrophotometer used was  
280 manufactured by Edinburgh Instruments Ltd. (range 0–10%; accuracy ±2%; digital resolution  
281 0.01%) pressure and temperature corrected and it is the same used in the surveys on Piton de la  
282 Fournaise volcano. The CO<sub>2</sub> flux is derived from the CO<sub>2</sub> dynamic concentration value through an  
283 empirical relationship (2) verified experimentally in the laboratory for a range of applicable  
284 permeability 0.36–123 μm<sup>2</sup> and pumping flux 0.4–4.0 L/min:

$$285 \quad CO_2 = (32 - 5.8 \cdot k^{0.24}) C_d + 6.3 \cdot k^{0.6} \cdot C_d^3 \quad (4)$$

286 where  $\phi_{CO_2}$  is the soil CO<sub>2</sub> flux expressed in kg m<sup>-2</sup> d<sup>-1</sup>, k is the numerical values of the gas  
287 permeability (μm<sup>2</sup>), and C<sub>d</sub> is the numerical value of molar fraction of the diluted CO<sub>2</sub>  
288 concentration. In this work,  $\phi_{CO_2}$  is converted into g m<sup>-2</sup> d<sup>-1</sup>. For more details on the method, see  
289 Camarda et al. [2006a, 2006b]. In this work we used a k value of 30, which is very close to the k  
290 value (35) used at Reunion island in previous studies on Piton de la Fournaise (Boudoire *et al.*,  
291 2017; Liuzzo *et al.*, 2013; Liuzzo et al., 2015). In consideration of the typical range of permeability  
292 in volcanic soils, k=30 value is a reasonable value limiting the error into less than 7% of the  
293 measurement (see table S1 supplementary materials).

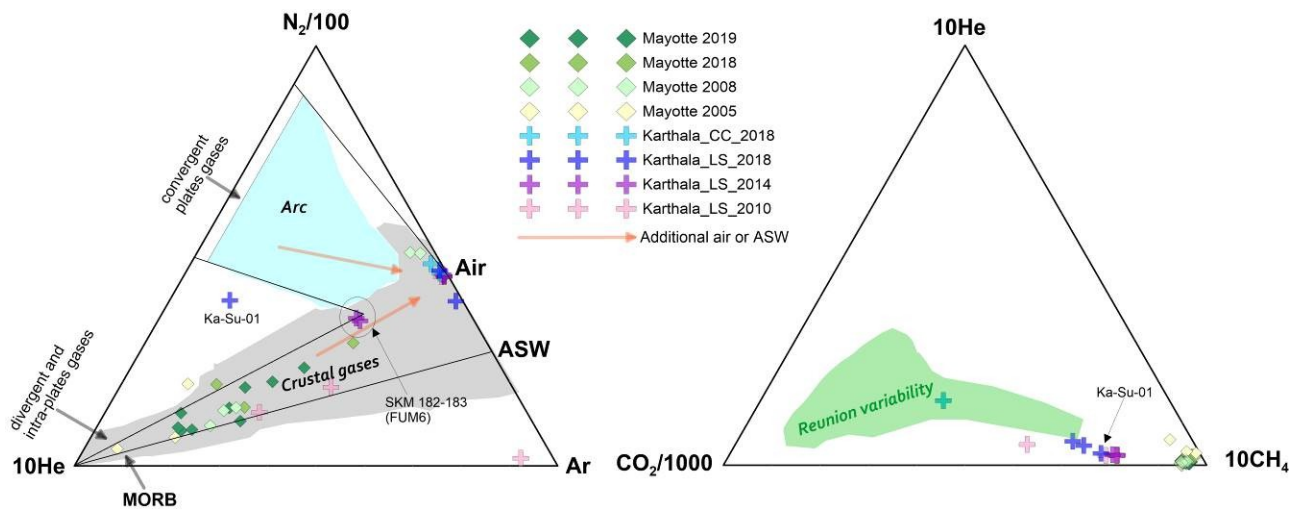
## 294 4. Results

### 295 4.1 Gas composition of fumaroles and bubbling gases

#### 296 4.1.1 Chemistry

297 Karthala gases (CC, from the summit caldera fumaroles; LS from the Soufrière area. For the  
298 locations see figure 5 and 6) show a general higher degree of air contamination with respect to  
299 Mayotte samples (table 3), with the exception of sample Ka-Su-01 from Soufrière that shows the  
300 highest CO<sub>2</sub> concentration (up to 92.2%), a significant content of H<sub>2</sub> (25,992 ppm), low  
301 concentrations of CH<sub>4</sub> (346 ppm). With regard to noble gases, He varies in a narrow concentration  
302 range (10.0-12.7 ppm), <sup>20</sup>Ne is between 0.03 (sample Ka-Su-01) and 7.7 ppm, <sup>40</sup>Ar 32.8 (sample Ka-  
303 Su-01) and 5,152.8 ppm. In the Mayotte sample set noble gases show a variable concentration,  
304 with He ranging between 8.2 and 113.2 ppm, <sup>20</sup>Ne between 0.052 and 7.65 ppm, <sup>40</sup>Ar in the range  
305 55.1-3346.6 ppm. Among the other samples taken from high flux pools, only the sample CI-1a has  
306 a significant air contamination, showing concentrations of N<sub>2</sub> and O<sub>2</sub> of 54.9% and 14.9%  
307 respectively. The BAS bubbling gases from the tidal flat show a CO<sub>2</sub> dominant composition up to  
308 98.69% and a variable concentration in CH<sub>4</sub> ranging between 416 and 2982ppm. The concentration  
309 of CH<sub>4</sub> increases significantly in the “MAN” samples, taken from low-flux pools located close to  
310 littoral mangroves (up to 4621 ppm). In the BAS samples, H<sub>2</sub> and CO are generally in low  
311 concentrations ranging between 2.2 and 318 ppm for H<sub>2</sub> and 0.7 and 18 ppm for CO.

312 The chemical composition of Karthala and Mayotte gases is plotted in the ternary diagrams of  
313 Figure 2. The relative proportions of N<sub>2</sub>, He and Ar, display a mixing trend between a He-rich  
314 component and a atmospheric component (air or air-saturated water – ASW). Both gases from the  
315 fumarolic Karthala areas (CC and LS) and the bubbling gases from Mayotte (BAS) show a variable  
316 degree of contamination by an atmospheric endmember, and its contribution is higher for air than  
317 for ASW. On the whole, the He-Ar-N<sub>2</sub> variability falls within a typical compositional range of crustal  
318 gases of which the two dominant mixing sources appear to be atmospheric and MORB-type  
319 mantle, well distinguished from typical subduction-related gases. An exception is the sample Ka-  
320 Su-01 which is significantly different from the present Karthala database, where only the samples  
321 SKM182 and SKM183 (fumarole 6 - survey 2014 Benavente et al. 2015) show some similarity in  
322 low <sup>40</sup>Ar and He/N<sub>2</sub> ratio. The chemical composition in relation to the plot of CO<sub>2</sub>-CH<sub>4</sub>-He highlights  
323 that low temperature gas seeps of Mayotte have a larger CH<sub>4</sub> proportion with respect to Karthala  
324 fumarolic gases. In the plot, it is also reported the field of variability of La Reunion bubbling gases  
325 that allows to argue that Comoros gases are in general CH<sub>4</sub>-enriched.



326

327 Figure 2. Relative proportion of He-Ar-N<sub>2</sub> in a ternary diagram on the left showing also the areas of crustal gases and  
 328 arc volcanism from literature. Data collected at Grande Comore and Mayotte show a variable air and ASW  
 329 contamination. CO<sub>2</sub>-CH<sub>4</sub>-He ternary diagram on the right displays a relatively CH<sub>4</sub>-enrichment of Grande Comore and  
 330 particularly in Mayotte. For comparison is also shown the field of variability of La Reunion gases.

#### 331 4.1.2 Isotopic ratios of noble gases, CO<sub>2</sub> and CH<sub>4</sub>

332

333 Table 1 reports the isotopic compositions of noble gases CO<sub>2</sub>, and CH<sub>4</sub> of the sampled gases.

334 Karthala gases have R/Ra values ranging from 3.8 (Ka-Su-02) and 5.71 Ra (Ka-Su-01), with an  
 335 overlap between CC and LS emissions. After correction for the contamination by atmospheric  
 336 fluids (Rc/Ra), the highest <sup>3</sup>He/<sup>4</sup>He value (5.72) is still measured in the sample Ka-Su-01, since it  
 337 has the minor air contamination. Instead, the other samples range from 5.4 to 5.9 Ra due to a  
 338 variable atmospheric contribution. In gases from Karthala, the <sup>4</sup>He/<sup>40</sup>Ar\* ratio calculated after the  
 339 correction of <sup>40</sup>Ar for atmospheric contamination (see eq. 2 in section 3.2) is available only for  
 340 sample Ka-Su-01 and is 1.4. The relatively higher air contamination in Karthala gases, than in  
 341 Mayotte gases, is also highlighted by the <sup>4</sup>He/<sup>20</sup>Ne (<sup>4</sup>He/<sup>20</sup>Ne<sub>air</sub>=0.318), which is generally low with  
 342 an average of 1.5 (with exception of Ka-Su-01, <sup>4</sup>He/<sup>20</sup>Ne = 356.58), and <sup>40</sup>Ar/<sup>36</sup>Ar (<sup>40</sup>Ar/<sup>36</sup>Ar<sub>air</sub>=295.5),  
 343 which is in average 303.2 (with exception of Ka-Su-01, <sup>40</sup>Ar/<sup>36</sup>Ar = 378).

344 In the BAS bubbling gases there is the lack of a strong air contamination as previously indicated by  
 345 the chemistry of these gases since the <sup>4</sup>He/<sup>20</sup>Ne ratios (up to 1663) are orders of magnitude higher  
 346 the ratio in air (0,318), therefore no significant changes can be observed in the comparison  
 347 between R/Ra and Rc/Ra values, except for only one sample (MAR-1) sampled in 2018. In fact, this  
 348 sample shows a <sup>3</sup>He/<sup>4</sup>He ratio of 3.2 Ra and a <sup>3</sup>He/<sup>4</sup>He ratio of 4.2 (Rc/Ra) after correction for air  
 349 contamination. The latter value strongly differs from the rest of the dataset of BAS gases, thus we  
 350 suspect that this sample underwent some storage and transport to the laboratory issues that

351 fractionated the  $^3\text{He}/^4\text{He}$ , leading us to exclude it for the following discussion. In support of this,  
352 we highlight that the sample MAR-3 collected in April 2019 from the same degassing area yielded  
353 an Rc/Ra value of 7.2 (Table 3). The  $^4\text{He}/^{40}\text{Ar}^*$  values of BAS gases range between 1.2 and 1.7 with  
354 a general overlap of the values among the different emissions and surveys.  $^4\text{He}/^{20}\text{Ne}$  in Mayotte  
355 samples vary up to 1660 and only the MAR-1 and MAN-2 ( $^4\text{He}/^{20}\text{Ne} = 1.07$  and 43.59, respectively)  
356 samples, both taken from pools with a relatively low flux, show significant air contamination. The  
357 variability of  $^{40}\text{Ar}/^{36}\text{Ar}$  span up to 434, with MAR-1 and MAN-2 again showing the highest air  
358 contamination ( $^{40}\text{Ar}/^{36}\text{Ar} = 290$  and 308, respectively).

359 The C-isotope composition of  $\text{CO}_2$  ( $\delta^{13}\text{C}_{\text{CO}_2}$ ) of Karthala gases varies between  $-4.98\text{‰}$  and  $-4.48\text{‰}$ ,  
360 except for sample Ka-Su-02 that shows the most positive value of  $-3.91\text{‰}$ . At Mayotte the  $\delta^{13}\text{C}_{\text{CO}_2}$   
361 values of BAS gases vary from  $-5.74\text{‰}$  and  $-3.5\text{‰}$ , whereas the most negative ratios are  
362 measured in samples from MAN.

363 The C and H pair isotope in methane were measured only in BAS gases. In detail, the C-isotope  
364 composition of  $\text{CH}_4$  ( $\delta^{13}\text{C}_{\text{CH}_4}$ ) was determined in most of the samples and varies between  $-24.4\text{‰}$   
365 and  $-18.7\text{‰}$ , except for two samples from MAN 1 and 2 that showed the less negative ratios of  $-$   
366  $12.4\text{‰}$  and  $-11.7\text{‰}$ . The  $\text{H}_2$ -isotope composition of  $\text{CH}_4$  ( $\delta\text{D}_{\text{CH}_4}$ ) was measured only in C1-2 and  
367 DIST-1 that were sampled in 2019 through Giggenbach bottles to enrich the concentration of  $\text{CH}_4$   
368 of dry gases. These samples yielded a  $\delta\text{D}$  of  $-118.1\text{‰}$  and  $-137.8\text{‰}$  V-SMOW, respectively.

369

## 370 5. Discussion

### 371 5.1 Light noble gas signature

372 Our new He-isotopic data for Karthala and Mayotte span a significant range of  $^3\text{He}/^4\text{He}$  signatures  
373 ( $4.18$ - $7.53$  Ra), with systematic differences between the two islands of Comoros archipelago. In  
374 detail, gases from Mayotte show Rc/Ra values higher than those from Karthala. Interestingly, the  
375 Rc/Ra variability we measured in 2017-2020 gases from Mayotte ( $7.5$ - $6.4$  Ra) and Karthala ( $5.9$ - $4.7$   
376 Ra) matches that found in fluid inclusions from the two active volcanic edifices of the Grande  
377 Comore, la Grille and the Karthala ( $6.9$  and  $5.2$  Ra respectively; Class et al., 2005). In Figure 3, we  
378 modelled two air-magma mixing curves considering data from Class et al. (2005) at Grande  
379 Comore and considering the average of the values for La Grille and Karthala fluid inclusions as  
380 representative of possible mantle reservoirs end-members. According to Class et al. (1998, 2005,  
381 2009) that propose the presence of a plume contribution in the mantle beneath Gran Comore, our  
382 data show that Comoros gases have a low-He signature, like the fluid inclusions in lavas from the

383 same volcanic systems (Karthala volcano). This low  $^3\text{He}/^4\text{He}$  signature is well distinct from that  
384 documented in typical hot-spot contexts like the adjacent Afar region (R/Ra up to 19.6; Marty et  
385 al., 1996; Hilton et al., 2011) and la Réunion (R/Ra = 14.5-12; Marty et al., 1993; Boudoire et al.,  
386 2020). In Figure 3, data of bubbling gases of Piton des Neiges from La Reunion are plotted together  
387 with two mixing curves that explain their variability, showing that they fall within the range of Rc/  
388 Ra values measured in fluid inclusions of eruptive products of the island.

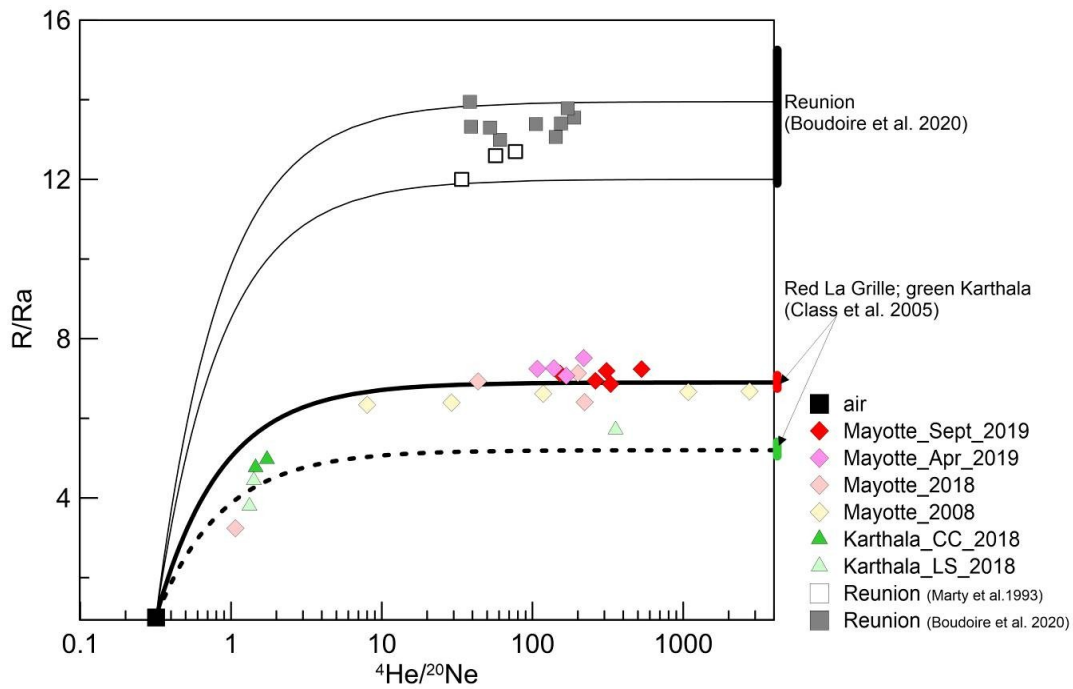
389 Ocean island basalts (OIB) from the Comoros archipelago display geochemical features different  
390 from the other Indian OIB [Späth et al. (1996), Class and Goldstein (1997), Class et al. (1998),  
391 Claude-Ivanaj et al. (1998), Deniel (1998), Class et al. (2009), Pelleter et al. (2014), Bachelery and  
392 Hemond (2016)]. Comoros volcanisms has produced a suite of variably silica-undersaturated,  
393 alkaline lavas (from melilitites and basanites, to alkali basalts to phonolites), enriched in  
394 incompatible trace elements and with variable relative depletion in K. With the exception of La  
395 Grille lavas, most lavas on the Archipelago record the signature of variable degrees of fractionation  
396 during their storage and ascent to the surface after their emission from the deep garnet-bearing  
397 mantle source (Bachelery et al., 2016). Several geochemical models have been proposed to explain  
398 the elongated array of their Sr-Nd-Pb isotopic signature, whose end-members range from i) mixing  
399 between heterogeneous deep plume sources (EMI, HIMU) and a shallower depleted convective  
400 ambient mantle or ii) mixing between a homogeneous deep plume sources (EMI component), plus  
401 a variable contribution of the shallower heterogeneous and old metasomatised oceanic  
402 lithosphere. Whatever the source of the mantle heterogeneities, all authors agree that Karthala  
403 lavas and rare old samples from Mayotte record the strongest EM1 contribution of the Comorian  
404 plume (Pelleter et al., 2014). According to Class et al. (1998), the alkali basalts of Karthala reflect  
405 mainly plume derived melts, while the basanites of La Grille are the products of interaction of  
406 plume melts with the metasomatised oceanic lithosphere. Class et al. (2005) show that olivines in  
407 Grande Comore lavas span a relatively small range of low- $^3\text{He}/^4\text{He}$  compositions. La Grille  
408 “lithosphere-dominated” lavas have preserved a nearly MORB signature ( $6.75\text{--}7.08 R_A$ ) suggesting  
409 that amphibole forming metasomatism occurred before the arrival of the plume. All samples show  
410 good correlations between Sr-Nd-He isotope ratios, indicating that the Grande Comore  $^3\text{He}/^4\text{He}$   
411 ratios are not significantly influenced by crustal contamination and reflect recent mixing between  
412 plume- and lithosphere-derived melts. These authors highlight that the deep plume component  
413 has a low and well constrained  $^3\text{He}/^4\text{He}$  signature of  $5.2 \pm 0.2 R_A$ . On the basis of the correlation  
414 with Osmium isotopes, Class et al. (2009) argue that the low-He signature does not record

415 contribution from subcontinental lithospheric mantle, but that of a deep plume interacting with  
416 oceanic lithosphere. In this frame, the Comoros plume would represent a “low  $^3\text{He}/^4\text{He}$  – high  
417  $^{187}\text{Os}/^{186}\text{Os}$ ” hotspot whose deep source is dominated by recycled  $^4\text{He}$ -rich material.

418 A detailed treatment of this topic is out of the scope of this paper and will be treated in ongoing  
419 studies. Whatever the specific process producing the low- $^3\text{He}/^4\text{He}$  signature, we show that  
420 Karthala gases record a signature consistent with that recorded in the fluid inclusions of its lavas.  
421 On the contrary, Mayotte gases have a slightly higher  $^3\text{He}/^4\text{He}$  signature, which matches that of la  
422 Grille lavas. These findings are consistent with the barometric results of previous works (Bachèlery  
423 et al., 2019; Berthod et al., 2020) on the lavas of Mayotte submarine eruption, showing that these  
424 evolved basanite magmas are extracted by large shallow mantle reservoirs (50-20 km depth)  
425 located between the Moho and the upper oceanic lithosphere.

426 The  $^4\text{He}/^{40}\text{Ar}^*$  values measured in Karthala (only one reliable value) and Mayotte gases vary in a  
427 narrow range (1.2-1.7), falling within that typical of fertile mantle ( $^4\text{He}/^{40}\text{Ar}^* = 1-5$ ; Marty, 2012)  
428 and magmatic values from other geodynamic settings (e.g., Paonita et al., 2012; Bräuer et al.,  
429 2013; Boudoire et al., 2018; Rizzo et al., 2019). In magmatic environments, this ratio varies during  
430 melts degassing and is indicative of relative entrapment pressures (e.g., Paonita et al., 2012;  
431 Boudoire et al., 2018). Focusing on Mayotte gases for which  $^4\text{He}/^{40}\text{Ar}^*$  is available for different gas  
432 emissions and surveys dates, we do not notice systematic variations. This leads us to two  
433 important deductions: the first is that this ratio is not modified by gas-water interaction as e.g. He/  
434  $\text{CO}_2$  (see section 5.2) and thus can be used to track temporal variations eventually related to  
435 changes in magmatic dynamics; the second is that Mayotte gas emissions reflect a magmatic  
436 degassing occurring in a narrow range of depth. In other words, we could consider a  
437 homogeneous (in terms of depth) source of degassing. If we consider the findings of a recent study  
438 carried out at La Reunion, in which Boudoire et al. (2018) constrained a range of  $^4\text{He}/^{40}\text{Ar}^* = 2.1 \pm 0.4$   
439 for fluids exsolved at underplating (10-15 km below Piton de la Fournaise), assuming a comparable  
440 ratio in primary magmas below Mayotte, we could speculate that BAS emissions reflect the  
441 degassing of a melt ponding at comparable depths. Finally, the lack of evident temporal variations  
442 leads us to consider limited depth variations of the melt feeding the discharge of BAS emissions.

443



444

445 Figure 3.  $^4\text{He}/^{20}\text{Ne}$  versus  $^3\text{He}/^4\text{He}$  (R/Ra) in fumaroles and bubbling gas from Grande Comore and Mayotte. For  
 446 comparison are shown data from bubbling gases at La Reunion from Boudoire et al., (2020) and Marty et al., (1993).  
 447 Thick and dash black lines indicating air-magma mixing are calculated from the average value [from Class et al.,  
 448 (2005)] of La Grille and Karthala fluid inclusions respectively. Thin black lines are calculated as the minimum and  
 449 maximum of bubbling gases at La Reunion. At the right side of the diagram are also indicated three solid black red and  
 450 green bars, corresponding to the range of the R/Ra variability of La Reunion, La Grille and Karthala fluid inclusions  
 451 respectively.

452

### 453 5.2 Evidences of gas-water interaction and origin of $\text{CO}_2$ and $\text{CH}_4$

454 To evaluate the carbon origin of  $\text{CO}_2$  in Karthala and Mayotte gases,  $\delta^{13}\text{C}$  is diagnostic of the  
 455 original geochemical environment, being able to discriminate between a magmatic source ( $-$   
 456  $8\text{‰} < \delta^{13}\text{C} < -4\text{‰}$ ; Sano and Marty, 1995), the contribution from subducted marine limestone with  
 457  $\delta^{13}\text{C}=0\text{‰}$ , and sedimentary rocks of organic origin with much lighter  $\delta^{13}\text{C}=-25\text{‰}$  (Hoefs, 2015).  
 458 Thus, we correlated the variation of the  $\text{CO}_2/{}^3\text{He}$  versus  $\delta^{13}\text{C}$  ratio based on the approach proposed  
 459 by Sano and Marty (1995 and references therein). Figure 4A plots two mixing curves modelled  
 460 considering both an organic and a limestone endmember, in which the mantle corresponds to  
 461  $\text{CO}_2/{}^3\text{He}= 5.0 \times 10^9$  and  $\delta^{13}\text{C}=-4.4\text{‰}$ , which result from the average values of our data and data from  
 462 literature. For both organic and limestone endmembers, a value of  $\text{CO}_2/{}^3\text{He}=1.0 \times 10^{13}$  is assumed,  
 463 whereas for organic and limestone  $\delta^{13}\text{C}$  endmember is assumed  $\delta^{13}\text{C}=-25\text{‰}$  and  $\delta^{13}\text{C}=0\text{‰}$   
 464 respectively (Sano and Marty, 1995). As known from other studies in hydrothermal gases (Capasso  
 465 et al., 2005; Gilfillan et al., 2009; Dubaqc et al., 2012; Rizzo et al., 2019), the  $\text{CO}_2/{}^3\text{He}$ ,  $\text{He}/\text{CO}_2$ ,  $\text{CH}_4/$   
 466  $\text{CO}_2$  ratios and  $\delta^{13}\text{C}$  isotopic signature can be potentially modified by gas-water interaction in

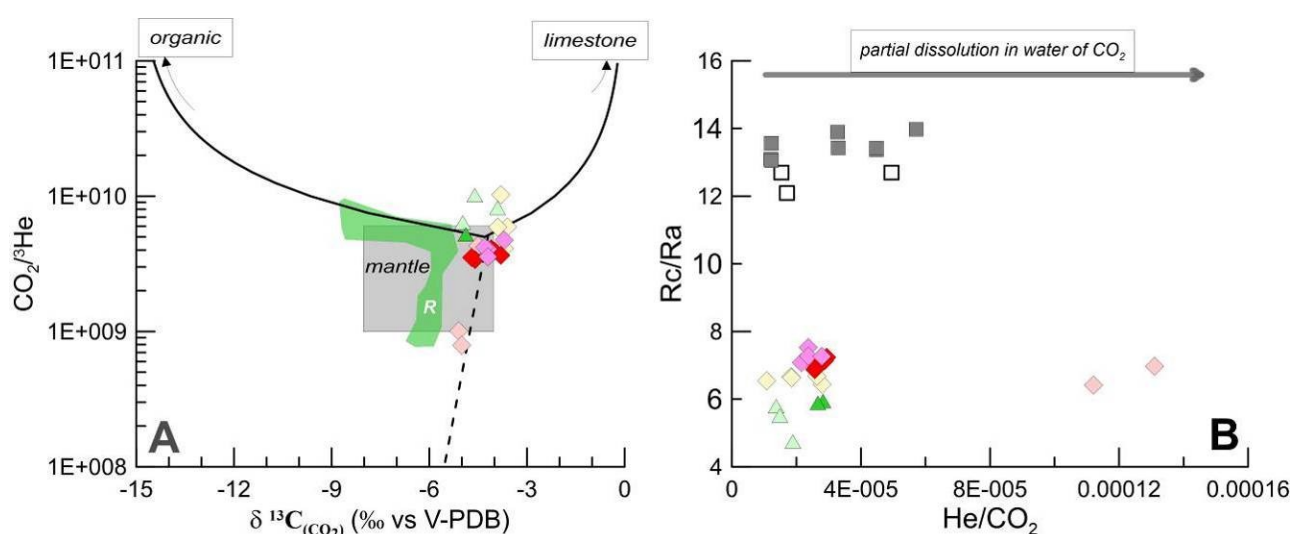
467 which CO<sub>2</sub> dissolves preferentially with respect to the other species. These effects need to be  
468 evaluated and eventually filtered out in order to calculate the thermobarometric conditions of the  
469 hydrothermal system feeding the gas seeps (Figures 2 and 4). In Mayotte gases, we observe only a  
470 modest variability of the He/CO<sub>2</sub> ratio (Figure 4), which overlaps with that found in Karthala fluids,  
471 with the exception of two 2018 samples from the “MAN” pools with low gas flux that show  
472 He/CO<sub>2</sub>>1.0x10<sup>-4</sup>. Similar evidences were observed by BRGM in 2005 samples 9a,b,c over the  
473 whole Mayotte tidal flat (Traineau, 2006) and might suggest an increase in gas fluxes after 2005. In  
474 order to constrain the pristine C isotopic signature of CO<sub>2</sub> in Karthala and Mayotte, we modelled a  
475 Rayleigh fractionation assuming a dissolution under equilibrium conditions based on the approach  
476 used in Rizzo et al. (2019). The Clark and Fritz (1997) equation is as follows:

$$477 \quad \delta^{13}C_{CO_2} = \epsilon \quad (5)$$

478 where the subscript 0 indicates the initial CO<sub>2</sub> isotope composition and  $f$  is the fraction of the  
479 residual gas phase, while  $\epsilon$  is the fractionation factor between DIC (dissolved inorganic carbon)  
480 and gaseous CO<sub>2</sub> (CO<sub>2(g)</sub>). In turn,  $\epsilon$  depends on water temperature and pH, which are unknown,  
481 therefore, for our purpose the values of temperature and pH has been chosen which better  
482 approximate our dataset corresponding to T=32°C and pH=5.71. These values correspond to those  
483 measured in the marine water of the Mayotte tidal flat by BRGM surveys (Traineau, 2006;  
484 Sanjouan, 2008). Our results show that Karthala gases are not evidently affected by interaction  
485 with shallow waters, as well as most Mayotte bubbling gases record only a minor partial  
486 dissolution of CO<sub>2</sub> (Figure S1 supplementary materials). The modest effect of preferential  
487 dissolution of CO<sub>2</sub> in water with respect to CH<sub>4</sub> and He is evident in Figure 4B, where He/CO<sub>2</sub> vs Rc/  
488 Ra are shown. Therefore, not considering the samples MAN affected by minor dissolution effects,  
489 the general variability of Mayotte and Karthala gases falls well within the range of mantle values  
490 (Figure 4A). In spite of streaming through a thick carbonate sequence of the coral reef or of the  
491 extensive bacterial contribution recorded in the nearby gas bubbling of the Dziani lake (Milesi et  
492 al., 2019, 2020), the gases of Mayotte tidal flat do not show any obvious limestone or organic  
493 contributions. Their magmatic signature can be constrained at  $\delta^{13}C \approx -4.3\text{‰}$ , which can also  
494 represent the magmatic signature of Karthala gases. This statement is supported by the narrow  
495 variability of  $\delta^{13}C$  range both at Karthala fumaroles ( $-4.9\text{‰} \leq \delta^{13}C \leq -3.9\text{‰}$ ) and Mayotte BAS high flux  
496 bubbling pools least affected by gas-water interaction ( $-4.9\text{‰} \leq \delta^{13}C \leq -3.5\text{‰}$ ), as well as by their  
497 relatively stability in time considering data from BRGM of 2006 and 2008 campaigns ( $-4.3\text{‰} \leq \delta^{13}C \leq$

498 3.2‰) as well as in 2016 with  $\delta^{13}\text{C} = -3.2\text{‰}$  (G7 point by Milesi et al., 2020). Therefore, a  $\delta^{13}\text{C} \approx$   
 499  $4.3 \pm 0.2\text{‰}$  is a reasonable approximation of a possible  $\delta^{13}\text{C}$  magmatic signature for the  
 500 Archipelago.

501 If compared to the bubbling springs of La Réunion (Figure 4A), we notice that the  $\delta^{13}\text{C}$  signature of  
 502 Mayotte and Karthala gases is slightly less negative and shows a minor variability. It is worth  
 503 noting that La Réunion gases with  $\delta^{13}\text{C} \approx -6\text{‰}$  display a trend of decrease of  $\text{CO}_2/{}^3\text{He}$  suggesting the  
 504 occurrence of a process of selective dissolution of  $\text{CO}_2$  in water, which is observed in Mayotte only  
 505 for the samples MAN 1 and 2.



506  
 507 Figure 4. A:  $\delta^{13}\text{C}$  of  $\text{CO}_2$  versus  $\text{CO}_2/{}^3\text{He}$  diagram of fumaroles and bubbling gases at Grande Comore and Mayotte. B:  
 508  $\text{He/CO}_2$  versus  $\text{Rc/Ra}$ . Symbols as in figure 3. For comparison is indicated also the variability of corresponding gases at  
 509 La Reunion (R). Diagram 4A shows that gases at Comore archipelago are in the field of Mantle-like origin with no  
 510 evident organic or limestone contributions. Solid lines are mixing curves between organic, mantle and limestone  
 511 endmembers, while the dashed line indicates a Rayleigh fractionation dissolution. Diagram 4B displays a variable  
 512 degree of water-gas interaction affecting  $\text{CO}_2$  variability.

513 Even if the Karthala and Mayotte fluids are  $\text{CO}_2$  dominated, we recall that they show a progressive  
 514 enrichment in  $\text{CH}_4$  up to concentrations of 2982 ppm in gases from Mayotte, which allowed to  
 515 measure its isotopic composition of C and H ( $\delta\text{D}$  of methane was measured only in DIST-1 and C1-  
 516 2, table 3). Following the classification proposed by Schoell (1980) (Figure S2 supplementary  
 517 materials), samples DIST-1 and C1-2 could be considered of abiogenic origin, coherently with the  
 518 G3 bubbling spot with the highest gas flux in the Dziani lake, recently documented by Milesi et al.  
 519 (2020) The same authors report of a G7 sample in the BAS area which shows similar  $\delta^{13}\text{C}$  of DIST-1  
 520 and C1-2 but very negative  $\delta\text{D}$  of methane ( $-250\text{‰}$ ). However, it must be stressed that  
 521 distinguishing between methanogenesis processes of biological origin or thermogenic processes at  
 522 the origin of  $\text{CH}_4$  (Mazzini et al, 2011; Schoell, 1980; Welhan, 1988) is complicated by possible

523 mixing between endmembers with different isotopic signature (Taran et al. 2010) or by the  
524 occurrence of oxidation processes (e.g., Batista Cruz et al., 2019). It is therefore clear that further  
525 data are needed to better constrain the origin of methane in the BAS area of Mayotte

526

### 527 5.3 CO<sub>2</sub> degassing from soil

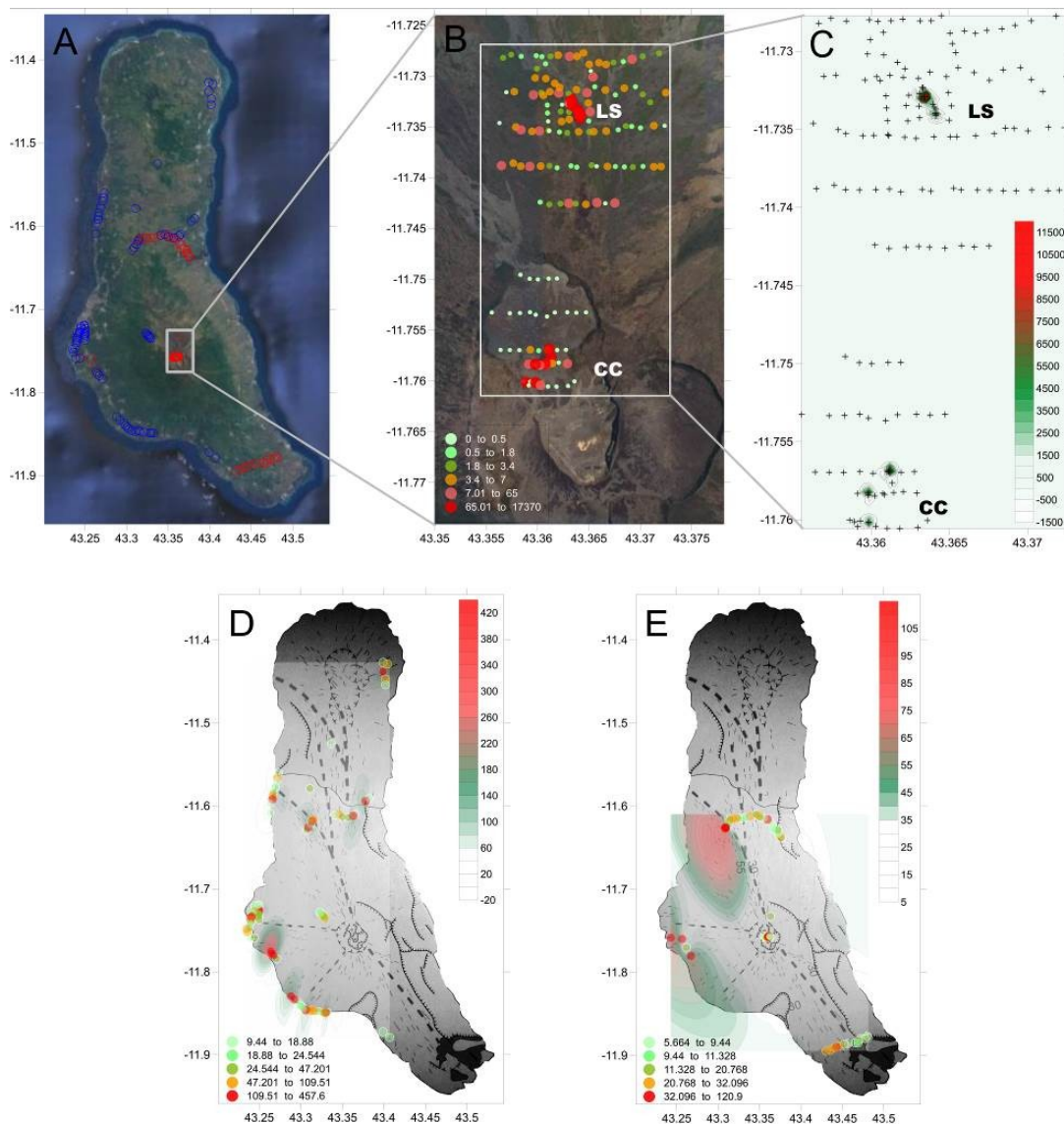
528 Volcanic areas are often places where diffuse outgassing of CO<sub>2</sub> emission occurs, facilitated by  
529 tectonic structures which locally increase soil permeability. On seismically and volcanically active  
530 areas like the Comoros, soil CO<sub>2</sub> emissions have been investigated in order to identify hidden  
531 tectonic structures driving fluid emissions to the surface (e.g., Bonforte et al., 2013; Boudoire et  
532 al., 2017; Giammanco et al., 2006; Gurrieri et al., 2008; Irwin and Barnes, 1980; Liuzzo et al., 2013).  
533 In volcanic tropical settings like the Comoros, the presence of significant fraction of soil CO<sub>2</sub>  
534 emissions can also be ascribed to biogenic activity, which may be mixed with gas originating from  
535 magmatic sources and whose relative proportion may evolve in time as a function of seasonal  
536 effects and the evolution of the seismic and volcanic activity (e.g., Boudoire et al., 2018a; Chiodini  
537 et al. 2008; Liuzzo et al., 2015).

538 While rift zones are marked by well defined alignments of volcanic cones in Grande Comore, they  
539 are much less defined in Mayotte, where a set of mafic scoria cones and phonolite maars are  
540 scattered on the Petite Terre island (Nehligh et al., 2013; Michon et al., 2016; Famin et al., 2020;  
541 Tzevahirtzian et al., 2021). In Grande Comore, volcano flanks are often resurfaced by the frequent  
542 emplacement of lava flows, nevertheless thick soils and sand covers are found in most locations,  
543 suitable for the measurement of soil CO<sub>2</sub> fluxes. At Petite Terre, the recent explosive activity of  
544 phonolitic maars emplaced a widespread cover of several meters thick fine grained ashes that,  
545 together with the low altitude of the island and the widespread urban context, limit the areas  
546 suitable for CO<sub>2</sub> flux measurements. In our survey strategy, we aimed at characterizing the CO<sub>2</sub>  
547 fluxes from the soil on the territory and linking them with known or hidden tectonic structures and  
548 with the main degassing areas (summit of Karthala in Grande Comore and Dziani lake and Airport  
549 tidal flat in Mayotte). Measurements on Mayotte tidal flat were performed at low tide, when the  
550 sandy/muddy flat is wet but without a continuous water cover, excepted some large bubbling  
551 pools. Samples of soil gas were taken alongside the soil CO<sub>2</sub> flux measurements to investigate the  
552 isotopic signature of carbon in CO<sub>2</sub> and thus constrain the sources of the soil CO<sub>2</sub> emission. As  
553 previously mentioned in 3.1, as the soil CO<sub>2</sub> dataset was acquired using two different methods and  
554 at different times, it is not uniform and therefore our choice in data analysis was to consider each

555 area separately. Even if acquired in different seasons and times, all the measurements were  
 556 carried out on dry sunny days and generally stable weather conditions. Where possible,  
 557 measurements were performed at a spacing of ca. 50 m or less, though in some cases distances  
 558 between individual sites and length and orientation of the tracks were dependent upon local  
 559 urban density, morphological obstacles, and vegetation cover.

### 560 5.3.1 Grande Comore

561 At Grande Comore three campaigns were conducted for the measurement of soil CO<sub>2</sub> using two  
 562 different methods: a) Accumulation chamber, b) Dynamic concentration (Figure 5).



563

564 Figure 5. Soil CO<sub>2</sub> measurements at Grande Comore. In A sites of measurements distinct in blue and red for 2017 and  
 565 2018 surveys respectively. Inside the white rectangular are indicated the 2018 sites of measurements not indicated in  
 566 B. In figure 7B a classed post map of the 2014 survey at the summit of Karthala volcano realized using the  
 567 accumulation chamber method. CC indicates the Central Caldera area; LS indicates La Sufriere. In C a contour plot of  
 568 soil CO<sub>2</sub> emission of the Karthala summit area. Figures 7D and E are related to 2017-2018 surveys respectively realized

569 using the “Dynamic concentration method” [Gurrieri and Valenza (1988)]. On both maps it has overlapped the  
570 structural map from Bachèlery and Coudray (1993).

571

572 The first survey at Grande Comore was conducted by Benavente et al. (2015) and focused on  
573 exploring the potential geothermal resources of the island. Using the accumulation chamber  
574 method (Chiodini et al., 1998), the survey concentrated on the summit area of Karthala volcano,  
575 providing a total of 155 measurements of CO<sub>2</sub> flux (table 2), and only a subset of measurements  
576 was performed on the volcano flanks showing very low soil degassing rates. In the summit caldera,  
577 the survey by Benavente et al. (2015) focused on the northern and recently active (2007) part of  
578 the caldera, consistently with previous geophysical and CO<sub>2</sub> surveys of Lénat et al. (1998) and  
579 Bernabeu et al. (2018), showing that the strongest hydrothermal activity occurs in this area (CC  
580 area). In addition, Benavente et al. (2015) provide the first dataset on the most active and high  
581 temperature Soufrière area, on the northern rift (LS area). The results of the 2014 survey are  
582 plotted in Figure 5 (B, C). The soil CO<sub>2</sub> flux ranges from background air (0 flux) up to 17,364 g/  
583 m<sup>2</sup>day. The grid of points in the area investigated by Benavente et al. (2015), was suitable for the  
584 estimation of the total budget of CO<sub>2</sub> flux emission at that period, resulting in an average of 288.8  
585 and 559.5 g/m<sup>2</sup>day at the crater and La Soufrière areas respectively. The remaining summit area  
586 investigated of Karthala volcano is characterized by a general very low average of CO<sub>2</sub> flux.

587 In 2017 and 2018, the second and the third soil CO<sub>2</sub> measurement surveys were carried out by  
588 IPGP and INGV teams, using the Dynamic method (Gurrieri and Valenza, 1988) and focusing on the  
589 volcano flanks and La Grille area. The unknown *k* value, necessary for the application of the  
590 dynamic method (equation 2), has been chosen from those which give the minimum percentage  
591 deviation between the most probable range of *k* values in volcanic soils (Camarda et al., 2006a)  
592 and in consideration of the similarity with soil CO<sub>2</sub> emission measured at La Reunion (Boudoire et  
593 al., 2017; Liuzzo et al., 2015). For all the measurements at Karthala a *k* value of 30 μm<sup>2</sup> has been  
594 chosen (see supplementary materials Table, S2). Considering reasonable that the probable range  
595 of permeability in volcanic soil ranges between 20 and 40 μm<sup>2</sup>, the percentage deviation is less  
596 than 6.5% in all the measurements carried out at Karthala.

597 87 measurements were taken during the 2017 campaign in the distal area of the Karthala volcano  
598 (table 1), with soil CO<sub>2</sub> flux ranging between approximately 9 and 450 g/m<sup>2</sup>day (table 2). During the  
599 2018 campaign, we carried out 65 measurements, where some were partially overlapping the  
600 previously surveyed area, however most were in new areas not covered by the 2017 survey

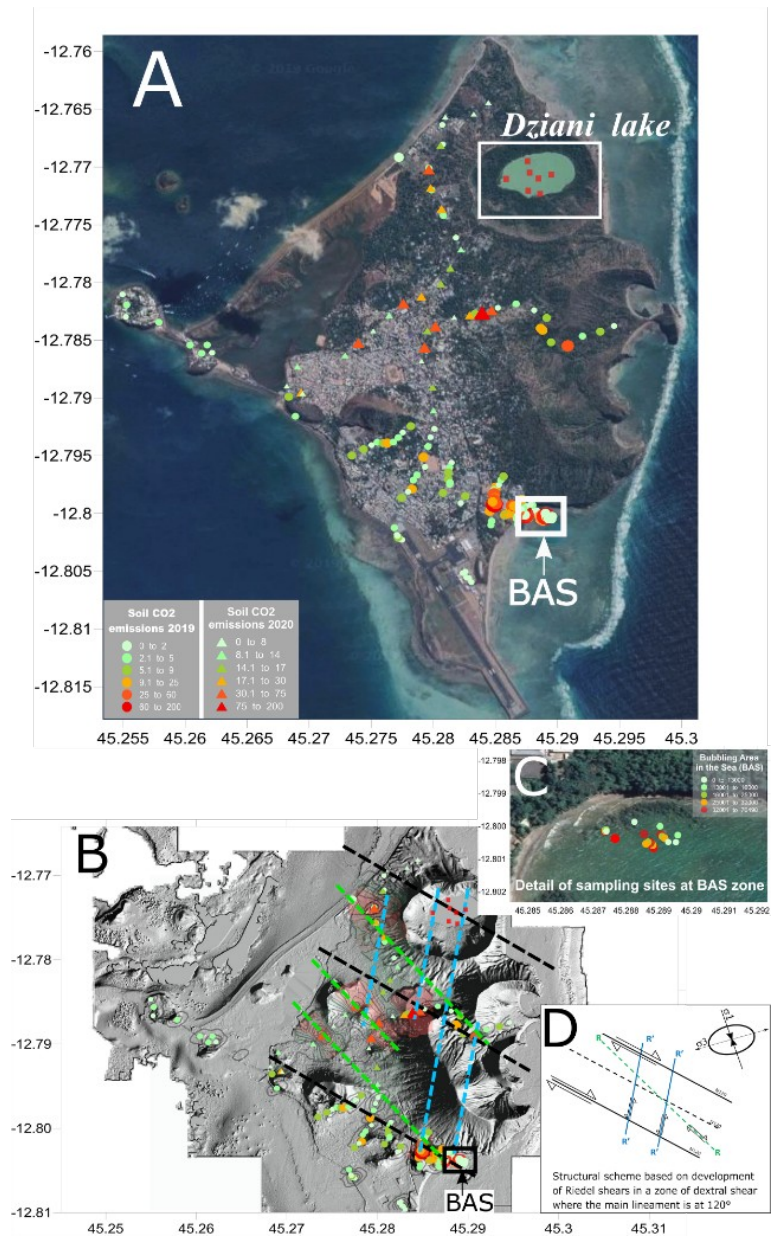
601 (Figure 7A). In 2018, minimum and maximum fluxes are around 5 and 950 g/m<sup>2</sup>day respectively,  
602 and confirmed that the maximum fluxes occur inside the summit caldera, close to the CC hot  
603 ground and fumarolic field. The findings of these two campaigns (Figure 5D and 5E) show a clear  
604 correlation between the main structures (Bachelery and Coudray, 1993) and the highest flux  
605 emissions, confirming that the spatial distribution of the soil CO<sub>2</sub> flux is tightly linked to the  
606 tectonic structures of Grande Comore. The Soufrière fumaroles and the maxima on the volcano  
607 flank fall on the main rift zones previously identified on the basis of the alignment of volcanic  
608 cone. Interestingly, anomalous areas of high CO<sub>2</sub> soil flux extend at low altitude, both in the  
609 northern and western part, where a recent seismic and volcanic activity has occurred, while very  
610 low fluxes are measured in the southern part of the island, which corresponds to the oldest little  
611 active part of Grande Comore (see Bachelery et al., 2016 for a recent review).

612 Soil gas fluxes and their spatial distribution reminds that documented on Piton de la Fournaise  
613 volcano where fluxes, in the range 5.52 to 701.56 g/m<sup>2</sup>day, have been measured during  
614 quiescence phases (Liuzzo et al., 2015). In spite of its strong eruption rate, Piton de la Fournaise  
615 lacks an area of strong degassing near its summit, which instead occurs on the older and quiescent  
616 Piton des Neiges volcano (Marty et al., 1993; Boudoire et al., 2020).

### 617 5.3.2 Mayotte - Petite Terre

618 The occurrence of a widespread ash cover makes the dynamic concentration method not suitable  
619 for most CO<sub>2</sub> flux measurements at Petite Terre, Mayotte, where surveys were performed using  
620 the accumulation chamber method in September 2019 and in November 2020 (Figure 6). On this  
621 island, a total of 166 measurements of CO<sub>2</sub> flux were taken from the soil and 53 on the tidal flat of  
622 the Airport (BAS: bubbling area in the sea Figure 6C). We did not perform a CO<sub>2</sub> survey inside the  
623 Dziani crater, however it represents a target of future investigations. Not surprisingly the strongest  
624 CO<sub>2</sub> soil emissions were measured in the Airport tidal flat, where the CO<sub>2</sub>-rich bubbling pools are  
625 located, with a range of values between 12 and 70,485 g/m<sup>2</sup>day. Peak emissions are thus 4 times  
626 higher than those measured at Karthala. The grid of points for this initial exploration did not lend  
627 itself to estimating the overall CO<sub>2</sub> flux budget, which will instead be the focus of future  
628 investigations. On land, we measured fluxes that span from background levels (corresponding to  
629 the air values concentrations) to 173.4 g/m<sup>2</sup>day, being much lower than in the volcano flanks of  
630 Karthala or of la Réunion. Our surveys show that at Mayotte the underlying hydrothermal system  
631 is the main source of the outgassing of the island and the bubbling area on the tidal flat is an  
632 important area of high CO<sub>2</sub> flux. This could arise from a combination of high fluxes focused in two

633 areas (Airport tidal flat and Dziani) and the widespread and poorly permeable fine ash cover on  
634 Petite Terre. The possible influence of the ash cover on soil CO<sub>2</sub> fluxes is however not  
635 straightforward. At Petite Terre, the thickness of fine ashes increases from west to east and the  
636 soil CO<sub>2</sub> fluxes as well, together with the occurrence of the two main areas of gas bubbling, which  
637 are located on the eastern side of the island. Even if the on land soil CO<sub>2</sub> emissions are generally  
638 modest compared with other sites, their spatial distribution still permits to identify preferential  
639 areas of CO<sub>2</sub> emissions on the ground and to discuss their possible link with hidden tectonic  
640 structures, not always recognisable with other methods of investigation. Available datasets  
641 (Tzevahirtzian et al., 2021; Famin et al., 2020) show that Petite Terre is the tip of a huge and  
642 mostly submarine volcanic ridge with a broad regional alignment in the N120° direction,  
643 corresponding to the main regional structure of Comoros archipelago and interpreted as a right-  
644 lateral shear in the lithosphere (Famin et al., 2020; Michon, 2016). Results from our surveys  
645 (Figure 6B) show a distribution of soil CO<sub>2</sub> degassing which might be overlapped to a possible  
646 structural scheme in which a system of fractures is determined by a combination of the main  
647 structural trends along N120° and a combination of Riedel's structures coherent with the right  
648 shear (Figure 6D). In this scheme, the N120° is well correlated to the alignment of Holocene  
649 tephritic scoria cones corresponding to the oldest phase of the recent volcanism of Petite Terre  
650 (Nehilg et al., 2013). A NNE-SSW (R') trend of soil CO<sub>2</sub> emission is overlapped on the most recent  
651 volcanism of the phonolitic maars, where the principal evidence of outgassing is shown by the BAS  
652 zone at the feet of the large "Vigie" maar and the bubbling manifestation inside the Dziani lake  
653 (Milesi et al., 2020). A possible trend corresponding to R structures is also appreciable in the  
654 central area of the island. Even if this first approach proposes an interpretative evaluation of the  
655 spatial outgassing distribution, however it must be stressed that future investigations on larger  
656 areas are needed to better understand the detailed structural pattern on Mayotte Island.



657

658 Figure 6. (A) Petite Terre (Mayotte) classed post map showing 2019 and 2020 surveys indicated as circles and triangles  
 659 respectively. Also shown inside the white rectangular at the Dziani lake (red squares) the bubbling area investigated by  
 660 Milesi et al., (2020). BAS indicates the bubbling area in the sea, which is magnified in (C) as a classed post map of the  
 661 CO<sub>2</sub> flux measurements carried out in 2019. In (B) digital elevation map of Petite Terre highlighting the volcanic cones  
 662 and the contour map of the soil CO<sub>2</sub> emissions. The structural trend in (B) is adapted to the Mayotte soil emissions  
 663 from the theoretical structural scheme exposed in figure (D) based on a dominant shear zone N120°.

664

#### 665 5.4 Equilibrium temperature of hydrothermal gases

666 In the previous paragraphs, we have shown that the fumarolic and bubbling gases of Grande  
 667 Comore and Mayotte have relatively high methane contents with the proportion of methane being  
 668 highest at Mayotte. We also highlighted the effect on gas chemistry of partial dissolution of CO<sub>2</sub> in  
 669 water, as well as identified the samples that showed the most evident effects of this process.

670 Data of CO<sub>2</sub> and CH<sub>4</sub> poorly or not affected by the dissolution of CO<sub>2</sub> in water allowed us to  
671 evaluate the possible gas equilibrium conditions among different gas species in hydrothermal  
672 environments. In several geothermal systems, the Fischer-Tropsch process has been successfully  
673 used to define the origin of methane since the 60s (D'amore and Panichi, 1980; Hulston and  
674 McCabe, 1962). Nowadays an extensive scientific literature exists that explores the conditions of  
675 equilibrium among gas species in hydrothermal environments in order to obtain useful geo-  
676 indicators for temperature and pressure (Chiodini and Marini, 1998; Fischer and Chiodini, 2015).  
677 Assuming that in the hydrothermal system an equilibrium is attained between the dominant  
678 species H<sub>2</sub>O-H<sub>2</sub>-CO<sub>2</sub>-CO-CH<sub>4</sub>, methane can form inorganically from the reaction:



680 where the formation of methane is favoured by the decreasing temperature. For this system we  
681 assumed as a condition of thermal equilibrium between CH<sub>4</sub> and CO<sub>2</sub> the equation proposed by  
682 Giggenbach (1992):

683 
$$\log (X_{\text{CH}_4} / X_{\text{CO}_2}) = 4625 / (t_e + 273) - 10.4 \quad (7)$$

684 where  $t_e$  is the equilibrium temperature (°C) while  $X_{\text{CH}_4}$  and  $X_{\text{CO}_2}$  are the molar fraction of CH<sub>4</sub> and  
685 CO<sub>2</sub> respectively.

686 Under these assumptions, equilibrium temperatures range between around 381 and 460°C at  
687 Karthala (Figures S2 supplementary m.) which is consistent with data from Benavente et al.,  
688 (2015). At Mayotte temperature vary between 314 and 339 °C (excluding MAN 1 and 2 which are  
689 recognized as affected by a severe dissolution of CO<sub>2</sub> in water). Interestingly, we do not record a  
690 change neither in equilibrium temperature nor in outlet temperature (in equilibrium with sea  
691 water temperature) in bubbling gases of the BAS Mayotte tidal flat in the period 2005-2019 in  
692 spite of the large magmatic event occurring at ca. 50 km from its coast.

693 To explore possible evidences of recent input of deep fluids in Mayotte hydrothermal system we  
694 evaluated the thermal equilibrium in combination with their isotopic signatures on the basis of  
695 their  $\delta^{13}\text{C}$  isotopic fractionation factor between CO<sub>2</sub> and CH<sub>4</sub>. In our BAS samples,  $\delta^{13}\text{C}_{\text{CH}_4}$  ranges  
696 from -24.4 to -11.7‰, the most positive values corresponding to the MAN samples collected by a  
697 low-flux pool close to the mangrove area (Figures S2 supplementary m.). To this aim, we have  
698 combined the temperatures obtained from (7) with the temperatures ( $t_e$ ) calculated using the  
699 equation proposed by Bottinga (1969) valid for temperatures ranging between 0-700 °C:

$$\Delta = 22166 / (t_e + 273) - 13.8 \quad (8)$$

701 where  $\Delta$  is the difference between  $\delta^{13}\text{C}_{\text{CO}_2}$  and  $\delta^{13}\text{C}_{\text{CH}_4}$  values. The relation (8) provides on the  
 702 whole higher temperatures, ranging between 370 and 515°C (Figures S2 supplementary  
 703 materials), where the samples MAN-1 and MAN-2 - (16-12-2018), which have been hypothesized  
 704 to be affected by a strong fluid-water interaction, provide a much higher apparent equilibrium  
 705 temperature up to 940°C and therefore they are not discussed further.

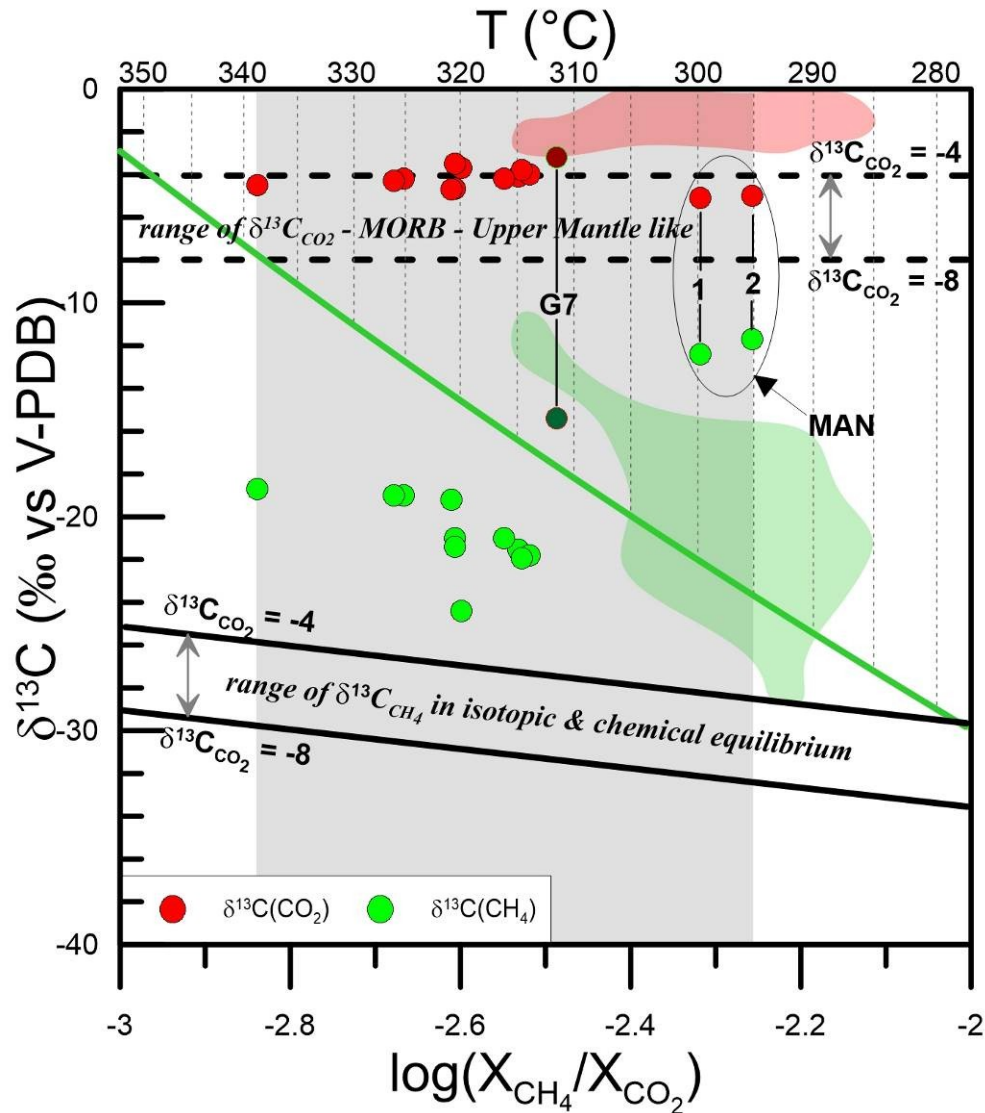
706 It is known that temperatures calculated from the  $\text{CO}_2\text{-CH}_4$  isotopic geothermometer are generally  
 707 higher than temperatures obtained from geothermometers based on chemical equilibrium (Horita,  
 708 2001). This difference is attributable to several process which can affect the final equilibrium and  
 709 various hypotheses have been invoked to account such outcomes. If external factors able to affect  
 710 the hydrothermal system cannot be excluded (e.g. an external sources of gas interacting with the  
 711 hydrothermal system) amongst the causes that might determine discrepancy on the estimation of  
 712 temperature, a sort of "quenching effect" on the isotopic signature of hydrothermal gases may be  
 713 considered relevant. Under this assumption,  $\text{CO}_2$  and  $\text{CH}_4$  were initially in isotopic equilibrium  
 714 attained at the original source (supposed to be deep) however, during the ascent of the gas to  
 715 shallow depths, there may not be enough time for the isotopic readjustment thus preserving the  
 716 original isotope ratios. Such a quenching effect is also justifiable by the faster rate of  
 717 reequilibration (about 100 times) of the chemical system than the isotopic system (Giggenbach,  
 718 1982).

719 In order to understand if the different temperature obtained by the chemical and isotopic  
 720 geothermometers could be an expression of a quenching effect acting on the BAS area at Mayotte  
 721 we plotted the log of the concentration ratio of  $\text{CH}_4$  and  $\text{CO}_2$  versus the  $\delta^{13}\text{C}$  of both methane and  
 722  $\text{CO}_2$  (Ono et al., 1993). In Figure 7 the thick black lines were modelled assuming that both chemical  
 723 and isotopic equilibrium is maintained with a fixed  $\delta^{13}\text{C}_{\text{CO}_2}$  corresponding to the range of magmatic  
 724 signature, here -4‰ and -8‰ (dashed black lines) by coupling the equations (7) and (8):

$$\log \left( \frac{X_{\text{CH}_4}}{X_{\text{CO}_2}} \right) = \frac{4625(\Delta + 13,8)}{22166} - 10,4 \quad (9)$$

726 In addition, the equilibrium temperature calculated using the equation (7) (green line) is shown.  
 727 The trend of the continuous black lines therefore should represent the variation of the  $\delta^{13}\text{C}_{\text{CH}_4}$   
 728 expected if equilibrium conditions are attained by gases injected in the hydrothermal system.  
 729 However, our data show a significant shift of the methane toward heavier isotopic concentrations.

730 Bacterial oxidation of thermogenic  $\text{CH}_4$  can explain isotopic fractionation determining an increase  
 731 of the isotopic ratio (Baker and Fritz, 1981; Coleman et al., 1981). For instance, this process may be  
 732 probable in the Dziani lake, where Milesi et al. (2020) have underlined a probable mixing between  
 733 gas of biogenic and magmatic origin.



734

735 Figure 7.  $\delta^{13}\text{C}$  for  $\text{CO}_2$  (red) and  $\text{CH}_4$  (green) versus  $\log(X_{\text{CH}_4}/X_{\text{CO}_2})$  of Mayotte bubbling gases. Dark red and green  
 736 symbols are referred to the G7 sample of Milesi et al., (2020) mentioned in the text, also the red and green area are  
 737 referred to the variability of the Dziani lake samples from the same authors. The green line correspond to the  $\text{CH}_4$  and  
 738  $\text{CO}_2$  thermal equilibrium expressed in equation (7) (Giggenbach, 1992), the thick black lines are calculated as the  
 739 equation (9) for isotopic and chemical equilibrium between  $\text{CH}_4$  and  $\text{CO}_2$  for two cases of  $\delta^{13}\text{C}(\text{CO}_2)$  corresponding at -  
 740 4‰ and -8‰ which in turn are indicated as dashed lines.

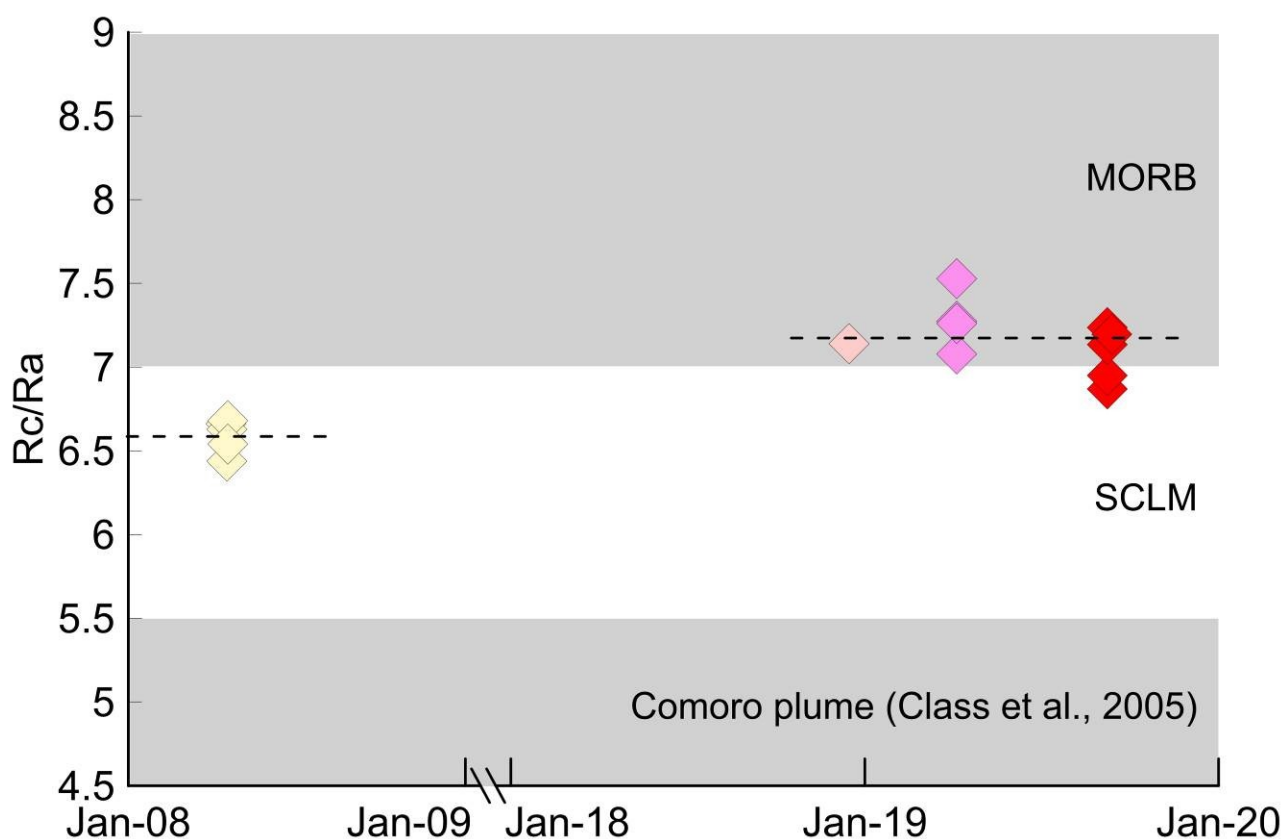
741

742 Although a carbon isotopic fractionation of methane cannot be excluded, some important  
 743 differences between the gases of the BAS area and Dziani Lake should be underlined. The range of  
 744 variability of  $\delta^{13}\text{C}_{\text{CH}_4}$  of the BAS samples is consistent with an abiogenic source (Schoell, 1980).

745 Moreover, the  $\delta D$  values of the samples DIST -1 and C1-2 are  $-137.8\text{‰}$  and  $-118.05\text{‰}$ ,  
746 respectively, being much higher than the value of G2 ( $-272\text{‰}$ ) methane-rich pool of Dziani lake  
747 reported by Milesi et al. (2020), confirming a probable abiotic origin of methane at BAS. Chemical  
748 equilibrium temperatures are systematically higher at BAS than at Dziani ( $<290^\circ\text{C}$ ), further  
749 suggesting an inorganic origin of BAS methane, or a more magmatic contribution in the hypothesis  
750 of a binary mixing between biotic and abiogenic methane. The methane-rich geochemical  
751 environment of the Dziani gases is definitely conditioned by the microbial activity in lacustrine  
752 waters, very different from the  $\text{CO}_2$ -rich geochemical environment of the BAS area. It is therefore  
753 likely that a quenching effect could explain the shift towards more positive  $\delta^{13}\text{C}$  values of methane  
754 in the BAS data that "freezes" the isotopic equilibrium at corresponding higher temperatures.  
755 Assuming that a quenching effect is significant on the BAS samples, the consequences are equally  
756 important; under this hypothesis the temperature would have a corresponding isotopic  
757 equilibrium in the range estimated by the equation (8), that is between  $370$  and  $515^\circ\text{C}$  and, in  
758 turn, such high temperatures can be explained by deep magmatic inputs.

### 759 5.5 Temporal variations of $^3\text{He}/^4\text{He}$ in gases from Mayotte

760 In order to have further evidences of possible variations of geochemical parameters that may have  
761 recorded the ongoing submarine volcanic activity, we evaluated the time variation of the helium  
762 isotope ratio. This tracer was found to be crucial in defining magmatic recharge in deep reservoirs  
763 in many volcanic systems on Earth (Boudoire et al., 2020; Caracausi et al., 2003; Sano et al., 2015;  
764 Paonita et al., 2016; Rizzo et al., 2015, 2016). Figure 6 shows values from the 2008 (BRGM  
765 repository) and the 2018-2019 surveys. As discussed before, the interpretation of this parameter is  
766 quite complex in the Comoros context, because of the possible "low- $^3\text{He}/^4\text{He}$ " signature of the  
767 deeper undegassed asthenospheric source. Our data suggests that the helium isotopic signature of  
768 the BAS fluids (Figure 8) was relatively low in the 2008 samples and it becomes significantly higher  
769 (average increase of  $0.58 \text{ Rc/Ra}$ ) in the samples from the 2018 survey. This shift is consistent with  
770 the drainage of large volumes of evolved basanite magma from shallow mantle lithospheric depth  
771 feeding the Mayote gaseous emissions at least in 2008, whose potential signature is very close to  
772 that recorded by fluid inclusions at La Grille (Class et al., 2005). Since the beginning of the  
773 eruption, the  $\text{Rc/Ra}$  signature of BAS fluids approaches that conventionally accepted for  
774 convective MORB mantle ( $8\pm 1 \text{ Ra}$ , Graham, 2002). Thus, we can tentatively speculate that this  
775 time evolution is associated with the emplacement of sub-lithospheric magmas at shallower depth  
776 along the large Mayotte volcanic ridge.



778

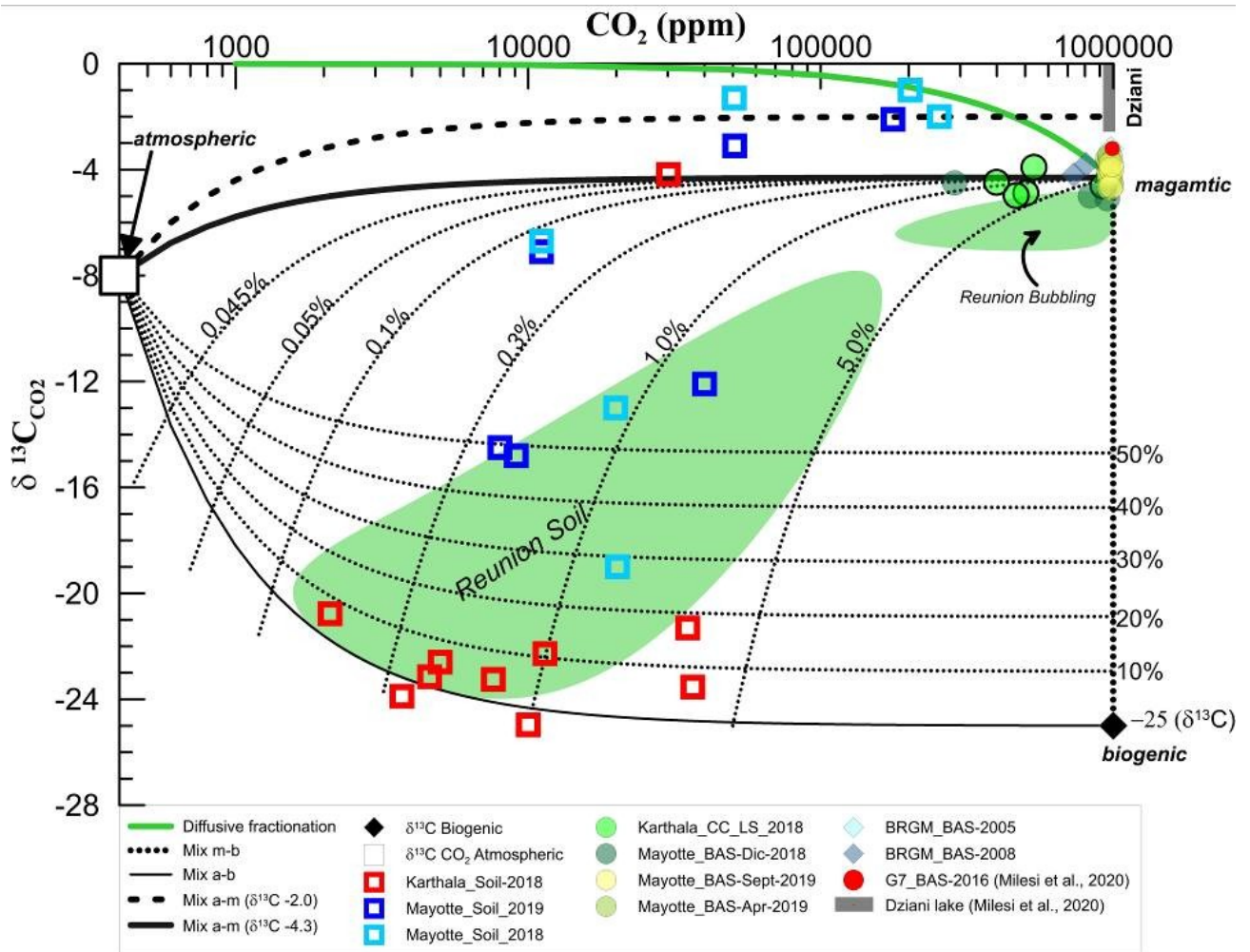
779 Figure 8. Rc/Ra time series with symbols as in figure 3. Rc/Ra has increased by an average 0.5 of between 2008 and  
 780 2018-2019. Black dashed lines indicate the averages Rc/Ra for the two distinct periods.

781

## 782 5.6 Gas emissions from the soil

783 Soil CO<sub>2</sub> emission can be ascribed to various origins and generally the total outgassing budget  
 784 results from a mixture of different sources (Amundson et al., 1998; Cerling et al., 1991; Chiodini et  
 785 al., 2008; Liuzzo et al. 2015). With the aim at quantifying the different contributions other than  
 786 those of magmatic origin, such as biogenic source or air contamination in soil CO<sub>2</sub> flux, 22 gas  
 787 samples were collected at Grande Comore and at Mayotte for CO<sub>2</sub> concentration and carbon  
 788 isotopic analysis ( $\delta^{13}\text{C}_{\text{CO}_2}$ ) (table 1). All the samples were taken directly at 0.5 m depth in the soil, as  
 789 described in section 3.2. The results of their CO<sub>2</sub> concentration and C isotopic signature are shown  
 790 in Figure 9, and are modelled as a mixing of three possible endmembers: atmospheric, biogenic  
 791 and magmatic. Figure 9 also reports  $\delta^{13}\text{C}$  of gas from fumarolic fields at Karthala (central crater CC  
 792 and La Soufrière LS, Figure 5B) and from the bubbling marine area off the coast at Mayotte (BAS,  
 793 Figure 6), both obtained from the 2017-2018 surveys. Included in Figure 9 are also data collected  
 794 at Mayotte by BRGM in 2005-2008 (BRGM/RP-568082 Final reports 2008) and in 2016 from Milesi  
 795 et al. (2020) at the Dziani volcanic lake, with the exception of sample G7 that was collected in 2016

796 at the bubbling area BAS. We report the endmembers of atmospheric ( $\delta^{13}\text{C} = -8\text{‰}$ ) and “biogenic”  
797 ( $\delta^{13}\text{C} = -25\text{‰}$ ; Hoefs, 2015) carbon (corresponding to organic matter). In Figure 9, we report the  
798 mixing curves between the three endmembers reported above. The effect of dissolution in water  
799 on the CO<sub>2</sub> emission from the soil, if any, is not included here, and in every cases it should be  
800 modest. The “magmatic” endmember was fixed considering the  $\delta^{13}\text{C}$  average values of CO<sub>2</sub> of  
801 fumarolic and bubbling gases from Karthala and Mayotte, which we considered representative of  
802 the magmatic signature beneath these islands of the Comore Archipelago ( $\delta^{13}\text{C}=-4.3\text{‰}$ ). This  
803 choice is supported by the small narrow variability of  $\delta^{13}\text{C}$  range of variation both in at Karthala  
804 fumaroles ( $-4.9\text{‰}\leq\delta^{13}\text{C}\leq-3.9\text{‰}$ ) and Mayotte BAS high flux bubbling pools least affected by gas-  
805 water interaction ( $-4.9\text{‰}\leq\delta^{13}\text{C}\leq-3.5\text{‰}$ , slightly higher values up to 5.7 being those of the MAN low  
806 flux pool), and their relatively stability in time considering data from BRGM of 2006 and 2008  
807 campaigns ( $-4.3\text{‰}\leq\delta^{13}\text{C}\leq-3.2\text{‰}$ ) as well as in 2016 with  $\delta^{13}\text{C}=-3.2\text{‰}$  (G7 point by Milesi et al.,  
808 2020), thus a reasonable approximation of a possible  $\delta^{13}\text{C}$  magmatic signature for the Archipelago.  
809 The effect of dissolution in water of the CO<sub>2</sub> emission from the soil it is not considered here  
810 because could be considered modest.



811

812 Figure 9. Diagram plotting carbon isotopic composition of soil  $CO_2$  versus soil  $CO_2$  log-concentrations (ppm) showing  
 813 the theoretical binary mixing curves between three endmembers: atmospheric, biogenic and magmatic. Also shown  
 814 are the binary mixing curves (hyphen curve) which allow a differentiation in the percentage of the magmatic  
 815 component (M) in the hypothesis that the biogenic contribution could be extended up to  $\delta^{13}C$  25‰ (Hoefs, 2015).  
 816 Green areas are referred to La Reunion soil and bubbling gases data repository, while the grey bar is the  $\delta^{13}C_{(CO_2)}$   
 817 Diziani lake's variability from Milesi et al., (2020).

818 The Karthala isotopic signature regarding  $\delta^{13}C$  in  $CO_2$  from the soil is much wider than in the  
 819 fumaroles and ranges in the interval  $-24.9\text{‰} \leq \delta^{13}C \leq -4.2\text{‰}$ . Almost all of the isotopic values show a  
 820 low contribution of magmatic  $\delta^{13}C$  and a variable degree of air contamination. A few samples  
 821 showing high  $CO_2$  concentration have however a modest magmatic contribution (less than 20%)  
 822 and correspond to sites close to the main structural lineaments showed in Figure 7. A single  $\delta^{13}C$   
 823 value from the soil at Karthala has an isotopic signature close to the magmatic endmember and  
 824 the corresponding site is very close to the steaming fumarolic field inside the summit CC caldera.  
 825 These results allow us to conclude that during the 2017 and 2018 surveys, which were performed  
 826 during a phase of quiescence of the volcano, soil  $CO_2$  emission on the flanks at Grande Comore was  
 827 predominantly of biogenic origin, while clear evidence of volcanic origin  $CO_2$  emission was  
 828 detectable only at the summit crater of Karthala. This overall picture of gas fluxes and isotopic

829 signature at Karthala is in strong contrast with that found during a similar quiescence period at  
830 Piton de la Fournaise (Liuzzo et al., 2015). On Piton de la Fournaise, only weak emission of low-  
831 temperature fluids and low CO<sub>2</sub> fluxes occur in the central summit area during quiescence periods,  
832 while diffuse CO<sub>2</sub> emissions with a clear and strong magmatic contribution (up to 60% of the  
833 diffuse fluid composition) have been detected along the main rift zones on the flanks of the  
834 volcano. On both volcanoes deep fluid percolation is focused on the main rift zones crossing the  
835 volcano edifice. However, the much lower rate of volcanic activity and longer quiescence duration  
836 at Karthala translates in low soil CO<sub>2</sub> fluxes with a dominant organic signature. The absence of  
837 permanent CO<sub>2</sub>-rich emissions below the summit area of Piton de la Fournaise has been attributed  
838 to the geometry of its deep plumbing system, which is laterally shifted with respect to the central  
839 summit area (Liuzzo et al., 2015; Michon et al., 2015).

840 At Mayotte the isotopic values of soil gases taken on land are much more scattered than the  
841 Karthala data sampled on the volcano flanks. The range of isotopic variation spans the  
842 19.0‰ ≤ δ<sup>13</sup>C ≤ -1‰ range at various CO<sub>2</sub> concentrations. In contrast with Karthala soil emissions,  
843 those from Mayotte show a significant magmatic contribution. It is interesting to notice a  
844 scattered distribution similar to that previously reported for δ<sup>13</sup>C in soil emission at La Reunion  
845 (Boudoire et al, 2017; Liuzzo et al, 2015). The Comoros archipelago is located in the Equatorial  
846 rainforest climate zone and La Réunion in a rainy tropical context. Therefore it is reasonable to  
847 consider that the soil of these islands is characterised by similar paedogenesis and biogenic  
848 processes to those identified in other tropical zones (Basile-Doelsch et al., 2005; Frank et al., 2002,  
849 2006; Rouff et al., 2012), which in turn can significantly affect the isotopic signature of carbon in  
850 soil CO<sub>2</sub>, as reported at La Reunion by Liuzzo et al. (2015). It is therefore not surprising that δ<sup>13</sup>C of  
851 CO<sub>2</sub> distribution in Mayotte lies within a comparable range of values as those reported for isotopic  
852 soil CO<sub>2</sub> measurements at La Reunion in previous works (Boudoire et al 2017, Liuzzo et al. 2015).  
853 Interestingly, in terms of soil emissions, the fluid composition and fluxes of Mayotte, where a huge  
854 submarine eruption is occurring, mimic those measured on the other very active volcano of the  
855 Indian ocean, Piton de la Fournaise.

856 The less negative δ<sup>13</sup>C values (-3‰ < δ<sup>13</sup>C < -1‰) were recorded at several soil CO<sub>2</sub> sampling areas  
857 that were taken on the beach or on a cliff very close to the BAS bubbling zone. However, these  
858 values cannot be explained as a mixing of atmospheric and magmatic CO<sub>2</sub> fixed at -4.3‰. The less  
859 negative δ<sup>13</sup>C values for these two sites elicit three possible hypotheses: either 1) they may lie in a

860 mixing curve between atmospheric and magmatic endmember where the magmatic signature is  
861 more positive (around  $\delta^{13}\text{C} = -2\text{‰}$ ); 2) they can be affected by isotopic fractionation on the aquifer;  
862 or 3) they are affected by kinetic fractionation due to a process of  $\text{CO}_2$  diffusion through the soil as  
863 observed in other studies (Capasso et al., 2001; Cerling, 1984; Hesterberg and Siegenthaler, 1991;  
864 Severinghaus et al., 1996). We stress that we identify this process only in a limited area, very close  
865 to the BAS tidal flat, which is affected by a process determining a significant modification of the  
866 isotopic signature that ends with less negative  $\delta^{13}\text{C}$  value. Regarding the first hypothesis, a mixing  
867 curve between air and magmatic endmember fixed at  $\delta^{13}\text{C} = -2\text{‰}$  seems to correlate well to these  
868 more positive isotopic data (black dashed curve in Figure 9). In addition, the mixing curve at  $\delta^{13}\text{C} = -$   
869  $2\text{‰}$  lies in the range of isotopic signatures of Dziani lake (Milesi et al., 2020). However, Dziani lake  
870 lies within a closed volcanic crater that receives a significant volcanic  $\text{CO}_2$  contribution. According  
871 to Milesi et al. (2019) also in such lacustrine site biogenic and microbial methanogenesis  $\text{CO}_2$   
872 reduction is particularly significant (thus potentially affecting the isotopic signature of  $\text{CO}_2$  shifting  
873  $\delta^{13}\text{C}$  toward more positive signature. These microbial processes have not been identified in our  
874 beach context. The similarity of the  $\delta^{13}\text{C}$  signature between Dziani lake and these few ground sites  
875 discussed is unrealistic also because the mentioned soil degassing area is far from Dziani lake,  
876 while instead very close to the BAS (a few tens of meters). As a consequence, we should expect an  
877 isotopic signature closer to that measured in BAS fluids. Moreover, it is difficult to explain  
878 alongside the entire dataset presented here, especially considering that the Karthala data fall  
879 within a range comparable to the bubbling data at Petite Terre. The second hypothesis invokes an  
880 isotopic fractionation that may be ascribed to the interference with the (salty) aquifer, which in  
881 turn should determine more negative isotopic values. In addition, the composition of soil gas  
882 samples collected at Mayotte do not show detectable  $\text{CO}_2$  dissolution in water (see Figure S1  
883 supplementary), therefore the interference of the aquifer at this site seems to be very modest.  
884 Regarding the third hypothesis, a curve of diffusive fractionation was modelled (green line in  
885 Figure 9) following Capasso et al. (2001):

$$886 \quad \delta_i = -\Delta_x \cdot \left( \frac{D_{j-a}}{D_{i-a}} - 1 \right) \cdot 10^3 \text{‰} \quad (9)$$

887 where  $\delta_i$  is the expected fractionated isotopic value of soil  $\text{CO}_2$  sample;  $\Delta_x$  is the variable molar  
888 fraction between  $\text{CO}_2$  in air and in the sample;  $D$  is the binary diffusion coefficient of  $\text{CO}_2$  in air;  
889 where specifically,  $D_j$  is related to  $^{12}\text{C}$ , and  $D_i$  is related to  $^{13}\text{C}$ . In our case, the diffusivity ratio of

890 carbon in CO<sub>2</sub> (by the way  $D_{j-a}/D_{i-a}$ ) is equal to 1.0044 (from Reid et al., 1977). For these samples,  
891 which were collected in the area close to the bubbling zone, it is therefore reasonable to consider  
892 a variable grade of isotopic diffusive fractionation that modified gases with a starting isotopic  
893 signature probably close to the bubbling gas thus leading to the conclusion that a kinetic diffusive  
894 fractionation might be the main process acting in this specific zone of the island.

895 We are aware that a wider dataset would certainly contribute to a more comprehensive  
896 understanding of the various processes responsible of the isotopic signature in soil CO<sub>2</sub> gas at  
897 Petite Terre. We however underline that the most significant results from this dataset support the  
898 hypothesis of a clear fingerprint of an active magmatic source into soil CO<sub>2</sub> emissions which has  
899 not been clearly identified on the volcano flanks of Karthala. Consequently, we conclude that the  
900 high CO<sub>2</sub> fluxes from the BAS tidal area and the time evolution of their He isotopic signature,  
901 together with the stronger magmatic CO<sub>2</sub> contribution emissions diffused on land at Petite Terre,  
902 potentially record the large magmatic and volcanic event occurring on the submarine flanks of the  
903 island. On the contrary, we can anticipate that the future reactivation of Karthala volcano should  
904 be recorded by a significant change in CO<sub>2</sub> emissions from the soil in terms of both fluxes, areal  
905 distribution and isotopic composition, as observed on other active volcanoes (Liuzzo et al. 2013).

## 906 6. Conclusion

907

908 This work presents the results of recent campaigns for the measurement of soil, fumarolic and  
909 bubbling gas emissions in two islands within the Comoros archipelago: Grande Comore and  
910 Mayotte. Although the measurement campaigns of soil CO<sub>2</sub> emissions are not exhaustive for the  
911 entire territory of these two islands, the first results show that they are spatially distributed along  
912 the main structural features of both Grande Comore and Petite Terre. A significant difference is  
913 found in the origin of the CO<sub>2</sub> emitted from the soil. The carbon isotopic signature of soil CO<sub>2</sub>  
914 emissions highlights evidence of a low magmatic contribution at distal areas of Karthala volcano,  
915 and a significantly higher magmatic contribution in CO<sub>2</sub> emissions at Petite Terre.

916 Gas geochemistry of fumarolic fields at Karthala (Grande Comore), and bubbling gases at Mayotte  
917 fall within the typical range of MORB-type mantle source. Compared with La Reunion dataset  
918 (Liuzzo et al., 2015; Boudoire et al., 2018), the Comoros islands dataset shows a CH<sub>4</sub> enrichment,  
919 and a variable degree of air contamination.

920 The isotopic signature of helium ( $^3\text{He}/^4\text{He}$ ) in gas emissions confirms relatively low Rc/Ra values  
921 (4.18-7.53) for the entire archipelago compared to other volcanic systems in the Indian Ocean  
922 such as Reunion (12-14.6).  $^3\text{He}/^4\text{He}$  data are consistent with average values of fluid inclusions for  
923 both Karthala and Petite Terre, spanning in the interval of  $6.41 \leq \text{Rc/Ra} \leq 7.53$  at Petite Terre and  
924  $4.68 \leq \text{Rc/Ra} \leq 5.87$  at Karthala. The origin of  $\text{CO}_2$  in the fumarolic emissions is basically magmatic  
925 (-5.7; -3.2) with no evidence of significant organic or sedimentary contribution for both Grande  
926 Comore and Mayotte.

927 Based on the  $\text{CO}_2$ ,  $\text{H}_2$ ,  $\text{H}_2\text{O}$  and  $\text{CH}_4$  contents, a hydrothermal system below Mayotte has been  
928 recognized with an equilibrium temperature of  $\sim 300^\circ\text{C}$ . Water-gas interaction process has been  
929 detected in Mayotte resulting in a partial  $\text{CO}_2$  dissolution in water. The methane of the  
930 hydrothermal system seems to be abiogenic in origin.

931 The differences recognized between Grande Comore and Mayotte may be ascribed to the different  
932 states of volcanic activity at the two islands at the time of the surveys. Soil  $\text{CO}_2$  emissions at  
933 Grande Comore are generally dominated by biogenic origin while there is a clear magmatic  $\text{CO}_2$   
934 contribution in Petite Terre.

935 Moreover, the increased value of Rc/Ra between 2008 and 2018-19 at Mayotte coupled to a not  
936 fully-reached isotopic equilibrium of the pair  $\delta^{13}\text{C}_{\text{CO}_2}$ - $\delta^{13}\text{C}_{\text{CH}_4}$  in the hydrothermal fluids may be  
937 ascribed to the recent volcanic activity which generated the new submarine volcano 45 km  
938 offshore from Petite Terre.

939 Further investigations and a suitable geochemical monitoring program are needed to better  
940 understand the complex volcanic system of Comoros archipelago. Nevertheless, our results show  
941 some clues of a potential volcano activity of Mayotte which opens important scenarios for the  
942 implication regarding procedures aimed to reduce volcanic hazard in this region.

#### 943 [Acknowledgments](#)

944 This work is part of the PhD (XXXIV cycle) of Marco Liuzzo at the University of Ferrara. The work  
945 has been partially founded by INGV (GECO project Fondi Ricerca libera 2019 INGV) and by  
946 REVOSIMA Initiative (IPGP, CNRS, BRGM, IFREMER) for fieldwork and analytical activities. We are  
947 grateful to CNDRS of Moroni for the local assistance to our team, as well as thankful to the  
948 Interreg Hatari support to A. Di Muro e B. Shafik. All datasets for this research are included in this  
949 paper (and its supplementary information files) and listed in tables 1-3 and table S1. Dataset not

950 included in the mentioned tables, which are showed in the figures 3, 4, 7, 9, S2, are available  
951 through the inside references cited and also listed in the final reference section.

952 The authors are very thankful to P. Allard for lending us the accumulation chamber for soil CO<sub>2</sub>  
953 surveys and C. Ventura Bordenga for his invaluable support on the Karthala field. We also thank  
954 INGV, Sezione di Palermo, for allowing the access to the analytical facilities. In particular, we are  
955 grateful to S. Cappuzzo who provided some of the technical equipment, F. Salerno and M. Longo  
956 for performing analyses of gases chemistry, M. Tantillo and M. Misseri for carrying out the noble  
957 gases isotopic measurements in the laboratory, G. Capasso, Y. Oliveri and A. Sollami for providing  
958 CO<sub>2</sub> and CH<sub>4</sub> isotopic analysis in the stable isotopes laboratory.

959

## 960 [References](#)

961 Amundson, R., Stern, L., Baisden, and Wang, Y. (1998) The isotopic composition of soil and soil-  
962 respired CO<sub>2</sub>, *Geoderma*, 82, 83–114

963 Bachelery, P., Berthod, C., Di Muro, A., Gurioli, L., Besson, P., Caron, B., ... & Jorry, S. (2019,  
964 December). Petrological and Geochemical Characterization of the Lava from the 2018-2019  
965 Mayotte Eruption: First Results. *AGU Fall Meeting Abstracts* (Vol. 2019, pp. V52D-06).

966 Bachèlery, P., and Hémond, C. (2016) Geochemical and Petrological Aspects of Karthala Volcano  
967 In: Bachèlery, P., Lénat, J.-F., Di Muro, A., Michon, L. (Eds.), *Active Volcanoes of the Southwest*  
968 *Indian Ocean: Piton de La Fournaise and Karthala*. *Springer-Verlag*, Berlin and Heidelberg, pp. 367–  
969 384

970 Bachèlery, P., Coudray, J. (1993) Carte volcano-tectonique (1/50000e) de la Grande Comore et  
971 notice explicative. Edited by the French Embassy in Moroni, Comoros, and The University of La  
972 Réunion, St. Denis de La Réunion

973 Bachèlery, P., Morin, J., Villeneuve, N., Soulé, H., Nassor, H. and Radadi Ali, A. (2016) Structure and  
974 Eruptive History of Karthala Volcano. In: Bachèlery, P., Lénat, J.-F., Di Muro, A., Michon, L. (Eds.),  
975 *Active Volcanoes of the Southwest Indian Ocean: Piton de La Fournaise and Karthala*. *Springer-*  
976 *Verlag*, Berlin and Heidelberg, pp. 345–366

977 Baker, J. F. and Fritz, P. (1981) Carbon isotope fractionation during microbial methane oxidation.  
978 *Nature* 293, 289-291

979 Basile-Doelsch, I., Amundson, R., Stone, W. E. E., Masiello, C. A., Bottero, J. Y., Colin, F., et al.  
980 (2005), Mineralogical control of organic carbon dynamics in a volcanic ash soil on La Reunion, *Eur.*  
981 *J. Soil Sci.*, 56, 689–703, doi:10.1111/j.1365-2389.2005.00703.x

982 Bassias, Y., & Leclaire, L. (1990) The Davie Ridge in the Mozambique Channel: crystalline basement  
983 and intraplate magmatism, *Neues Jahrbuch für Geologie und Paläontologie*, 4, 67–90

984 Batista Cruz, R. Y., Rizzo, A. L., Grassa, F., Bernard Romero, R., González Fernández, A.,  
985 Kretzschmar, T. G., & Gómez–Arias, E. (2019). Mantle degassing through continental crust  
986 triggered by active faults: The case of the Baja California Peninsula, Mexico. *Geochemistry,*  
987 *Geophysics, Geosystems*, 20. <https://doi.org/10.1029/2018GC007987>

988 Benavente, O., and Brotheridge, J. (2015) Comoros surface exploration. Geochemistry, soil CO2  
989 flux and shallow temperature surveys. New Zealand Ministry of Foreign Affairs and Trade (MFAT).  
990 Jacobs. 65pg.

991 Bernabeu, N., Finizola, A., Smutek, C., Saramito, P., & Delcher, E. (2018). Spatio-temporal evolution  
992 of temperature and fluid flow through a new “thermo-lithological” boundary; the case of a pit  
993 crater of Karthala volcano (Comoros archipelago) refilled on January 13th 2007 by a lava flow.  
994 *Journal of Volcanology and Geothermal Research*, 367, 7-19.  
995 <https://doi.org/10.1016/j.jvolgeores.2018.10.013>

996 Berthod, C., Médard, E., Bachèlery, P., Gurioli, L., Di Muro, A., Peltier, A., ... & Feuillet, N. (2020,  
997 December). The 2018-ongoing Mayotte submarine eruption: magma migration imaged by  
998 petrological monitoring. *AGU Fall Meeting*, 1-17 décembre 2020.

999 Bonforte, A., Federico, C., Giammanco, S., Guglielmino, F., Liuzzo, M., Neri, M., 2013. Soil gases  
1000 and SAR measurements reveal hidden faults on the sliding flank of Mt. Etna (Italy). *J. Volcanol.*  
1001 *Geotherm. Res.* 251, 27–40

1002 Bottinga, Y. (1969) Calculated fractionation factors for carbon and hydrogen isotope exchange in  
1003 the system calcite-carbon dioxide-graphite-methane hydrogen-water vapor. *Geochim. Cosmochim.*  
1004 *Acta* 33, 49-64

1005 Boudoire, G., Finizola, A., Di Muro, A., Peltier, A., Liuzzo, M., Grassa, F., et al. (2018a) Small-scale  
1006 spatial variability of soil CO2 flux: Implication for monitoring strategy. *Journal of Volcanology and*  
1007 *Geothermal Research*. Volume 366. ISSN 0377-0273.  
1008 <https://doi.org/10.1016/j.jvolgeores.2018.10.001>

1009 Boudoire, G., Liuzzo, M., Di Muro, A., Ferrazzini, V., Michon, L., Grassa, F., Derrien, A., et al. (2017)  
1010 Investigating the deepest part of a volcano plumbing system: evidence for an active magma path  
1011 below the western flank of Piton de la Fournaise (La Reunion Island). *J. Volcanol. Geotherm. Res.*  
1012 <https://doi.org/10.1016/j.jvolgeores.2017.05.026>

1013 Boudoire G., Rizzo, A. L., Di Muro, A., Grassa, F. & Liuzzo, M. (2018b) Extensive CO<sub>2</sub> degassing in  
1014 the upper mantle beneath oceanic basaltic volcanoes: First insights from Piton de la Fournaise  
1015 volcano (La Réunion Island). *Geochimica et Cosmochimica Acta* 235, 376–401

1016 Boudoire G., Rizzo, A.L., Arienzo, I. et al. (2020) Paroxysmal eruptions tracked by variations of  
1017 helium isotopes: inferences from Piton de la Fournaise (La Réunion island). *Sci Rep* 10, 9809  
1018 (2020). <https://doi.org/10.1038/s41598-020-66260-x>

- 1019 BRGM/RP-568082 Final reports 2008 – Sanjuan, B., Baltassat, J. F. – Estimation du potentiel  
1020 géothermique de Mayotte: Phase 2 – Etape 2. Investigations.-M., Bezalgues S., Brach M., Girard J.-  
1021 F., Mathieu géologiques, géochimiques et géophysiques complémentaires, synthèse des résultats
- 1022 Camarda, M., Gurrieri, S., and Valenza, M. (2006a) CO<sub>2</sub> flux measurements in volcanic areas using  
1023 the dynamic concentration method: Influence of soil permeability, *J. Geophys. Res.*, 111, B05202,  
1024 Doi:10.1029/2005JB003898
- 1025 Camarda, M., Gurrieri, s., and Valenza, M. (2006b), In situ permeability measurements based on a  
1026 radial gas advection model: Relationships between soil permeability and diffuse CO<sub>2</sub> degassing in  
1027 volcanic areas, *Pure Appl. Geophys.*, 163(4), 897–914, doi:10.1007/s00024-006-0045-y
- 1028 Capasso, G., D’Alessandro, W., Favara, R., Inguaggiato, S., Parello, F. (2001) Kinetic isotope  
1029 fractionation of CO<sub>2</sub> carbon due to diffusion processes through the soil. *Water-Rock Interaction*  
1030 10. Swets & Zeitlinger, Lisse
- 1031 Caracausi A., Italiano, F., Paonita, A., Rizzo, A., and Nuccio, P. M. (2003), Evidence of deep magma  
1032 degassing and ascent by geochemistry of peripheral gas emissions at Mount Etna (Italy):  
1033 Assessment of the magmatic reservoir pressure, *J. Geophys. Res.*, 108(B10), 2463,  
1034 doi:10.1029/2002JB002095
- 1035 Cerling, T.E. (1984) The stable isotopic composition of modern soil carbonate and its relationship  
1036 to climate Earth. *Planet. Sci. Lett.*, 71 (1984), pp. 229-240
- 1037 Cerling, T. E., Solomon, D. K., Quade, J., and Bowman, J. R. (1991) On the isotopic composition of  
1038 carbon in soil carbon dioxide, *Geochim. Cosmochim. Acta*, 55, 3403–3405
- 1039 Cesca, S., Letort, J., Razafindrakoto, H. N., Heimann, S., Rivalta, E., Isken, M. P., Nikkhoo, M.,  
1040 Passarelli, L., Petersen, G. M., Cotton, F., & Dahm, T., 2020. Drainage of a deep magma reservoir  
1041 near Mayotte inferred from seismicity and deformation. *Nature Geoscience*, 13(1), 87-93
- 1042 Chaheire, M., Chamassi, M., and Houmadi, N. (2016) GEOTHERMAL DEVELOPMENT IN THE  
1043 COMOROS AND RESULTS OF GEOTHERMAL SURFACE EXPLORATION - Proceedings, *6th African Rift*  
1044 *Geothermal Conference Addis Ababa, Ethiopia, 2nd – 4th November 2016*
- 1045 Chiodini, G., Cioni, R., Guidi, M., Marini, L. & Raco, B. (1998) - Soil CO<sub>2</sub> flux measurements in  
1046 volcanic and geothermal areas. *Appl. Geochem.*, 13, 534–552
- 1047 Chiodini, G. and Marini, L. (1998), Hydrothermal gas equilibria: The H<sub>2</sub>O-H<sub>2</sub>-CO<sub>2</sub>-CO-CH<sub>4</sub> system,  
1048 *Geochim. Cosmochim. Acta.* 62, 2673–2687
- 1049 Chiodini, G., Caliro, S., Cardellini, C., Avino, R., Granieri, D., and Schmidt, A. (2008), Carbon isotopic  
1050 composition of soil CO<sub>2</sub> efflux, a powerful method to discriminate different sources feeding soil  
1051 CO<sub>2</sub> degassing in volcanic-hydrothermal areas, *Earth Planet. Sci. Lett.*, 274(3–4), 372–379,  
1052 doi:10.1016/j.epsl.2008.07.051

- 1053 Clark, I. D., and Fritz, P. (1997). Environmental Isotopes in Hydrogeology. Boca Raton, FL: CRC  
1054 Press, 328
- 1055 Class, C, Goldstein, S.L. (1997) Plume-lithosphere interactions in the ocean basins: constraints from  
1056 the source mineralogy. *Earth Planet Sci Lett* 150:245–260
- 1057 Class, C, Goldstein, S.L., Altherr, R., Bachelery, P. (1998) The process of plume—lithosphere  
1058 interactions in the Ocean Basins—the case of Grande Comore. *J Petrol* 39(5):881–903
- 1059 Class, C., Goldstein, S.L., Shirey, S.B. (2009) Osmium in Grande Comore lavas: a new extreme among  
1060 a spectrum of EM-type mantle endmembers. *Earth Planet Sci Lett* 284:219–227
- 1061 Class, C., Goldstein, S.L., Stute, M., Kurz, M.D., Schlosser, P. (2005) Grand Comore Island: a well-  
1062 constrained “low 3He/4He”. *Earth Planet Sci Lett* 233:391–409
- 1063 Claude-Ivanaj, C., Bourdon, B., Allègre, C.J. (1998) Ra-Th-Sr isotope systematic in Grande Comore  
1064 Island: a case study of plume-lithosphere interaction. *Earth Planet Sci Lett* 164:99–117
- 1065 Coffin, M. F., Rabinowitz, P. D., & Houtz, R. E., (1986). Crustal structure in the western Somali  
1066 Basin. *Geophysical Journal International*, 86(2), 331-369
- 1067 Coleman, D. D., Risatti, J. B. and Schoell, M. (1981) Fractionation of carbon and hydrocarbon  
1068 isotopes by methane-oxidizing bacteria. *Geochim. Cosmochim. Acta* 45, 1033-1037
- 1069 Coltorti, M., Bonadiman, C., Hinton, R.W., Siena, F., Upton, B.G.J. (1999) Carbonatite  
1070 metasomatism of the oceanic upper mantle: evidence from clinopyroxenes and glasses in  
1071 ultramafic xenoliths of Grande Comore, Indian Ocean. *J. Petrol* 40:133–165
- 1072 Courtillot, V., Davaille, A., Besse, J., Stock, J. (2003) Three distinct types of hotspots in the Earth’s  
1073 mantle. *Earth Planet Sci Lett* 205:295–308
- 1074 D’Amore, F., and Panichi, C. (1980). Evaluation of deep temperature of hydrothermal systems by a  
1075 new gas geothermometer. *Geochim. Cosmochim. Acta* 44, 549–556. doi: 10.1016/0016-  
1076 7037(80)90051-4
- 1077 Debeuf, D. (2004) Etude de l’évolution volcano-structurale et magmatique de Mayotte (Archipel  
1078 des Comoros, Océan Indien): Approches structurale, pétrographique, géochimique et  
1079 géochronologique. Unpublished Ph.D. thesis, Université de La Réunion, 243 pp
- 1080 Deniel, C. (1998) Geochemical and isotopic (Sr, Nd, Pb) evidence for plume-lithosphere  
1081 interactions in the genesis of Grande Comore magmas (Indian Ocean). *Geochem Geol* 144:281–303
- 1082 Emerick, C.M., & Duncan, R.A. (1982) Age progressive volcanism in the Comoros Archipelago,  
1083 eastern Indian Ocean and implications for Somali plate tectonics, *Earth Planet Sci Lett* 60(3), 415–  
1084 428
- 1085 Evans, W.C, Sorey, M.L., Kennedy, B.M., Stonestrom, D.A., Rogie, J.D., Shuster, D.L. (2001) High  
1086 CO<sub>2</sub> emissions through porous media: transport mechanisms and implications for flux

1087 measurement and fractionation. *Chemical Geology*, Volume 177, Issues 1–2, 2001, Pages 15-29,  
1088 ISSN 0009-2541, [https://doi.org/10.1016/S0009-2541\(00\)00379-X](https://doi.org/10.1016/S0009-2541(00)00379-X)

1089 Famin, V., Michon, L., & Bourhane, A., 2020. The Comoros archipelago: a right-lateral transform  
1090 boundary between the Somalia and Lwandle plates. *Tectonophysics*,  
1091 [doi.org/10.1016/j.tecto.2020.228539](https://doi.org/10.1016/j.tecto.2020.228539)

1092 Feuillet, N. et al., 2019. Birth of a large volcano offshore Mayotte through lithosphere-scale  
1093 rifting, in *Proceedings of the AGU Fall Meeting 2019*. AGU

1094 Fischer, T. P., and Chiodini, G., 2015. Volcanic, magmatic and hydrothermal gases. In *The*  
1095 *Encyclopedia of Volcanoes*, 2nd edn. *Academic Press, Elsevier, Waltham*, pp. 779–796,  
1096 [doi:10.1016/B978-0-12-385938-9.00045-6](https://doi.org/10.1016/B978-0-12-385938-9.00045-6)

1097 Frank, A. B., Liebig, M. A., and Hanson, J. D. (2002), Soil carbon dioxide fluxes in northern semiarid  
1098 grasslands, *Soil Biol. Biochem.*, 34, 1235–1241. Frank, A. B., M. A. Liebig, and D. L. Tanaka (2006),  
1099 Management effects on soil CO<sub>2</sub> efflux in northern semiarid grassland and cropland, *Soil Tillage*  
1100 *Res.*, 89, 78–85, [doi:10.1016/j.still.2005.06.009](https://doi.org/10.1016/j.still.2005.06.009)

1101 French, S. W., & Romanowicz, B. (2015). Broad plumes rooted at the base of the Earth's mantle  
1102 beneath major hotspots. *Nature*, 525(7567), 95-99.

1103 Gaina, C., Torsvik, T. H., van Hinsbergen, D. J. J., Medvedev, S., Werner, S. C., and Labails, C. (2013),  
1104 The African Plate: A history of oceanic crust accretion and subduction since the Jurassic,  
1105 *Tectonophysics*, 604, 4–25

1106 Gérard, E., De Goeyse, S., Hugoni, M., Agogué, H., Richard, L., Milesi, V., et al. (2018). Key role of  
1107 alphaproteobacteria and cyanobacteria in the formation of stromatolites of Lake Dziani Dzaha  
1108 (Mayotte, Western Indian Ocean). *Frontiers in microbiology*, 9, 796.

1109 Giammanco, S., Gurrieri, S., and Valenza, M. (2006), Fault controlled soil CO<sub>2</sub> degassing and  
1110 shallow magma bodies: Summit and lower East Rift of Kilauea Volcano (Hawaii), 1997, *Pure Appl.*  
1111 *Geophys.*, 163(4), 853–867, [doi:10.1007/s00024-006-0039-9](https://doi.org/10.1007/s00024-006-0039-9)

1112 Giggenbach, W. F. (1982) Carbon-13 exchange between CO<sub>2</sub> and CH<sub>4</sub> under geothermal  
1113 conditions. *Geochim. Cosmochim. Acta* 46, 159-165

1114 Giggenbach, W. F. (1992) Chemical techniques in geothermal exploration. Applications of  
1115 geochemistry in geothermal reservoir development (F. D'Amore ed.) UNITAR/UNDP Centre on  
1116 Small Energy Resources. pp. 119-143, Rome

1117 Giggenbach, W.F., and Goguel, R.L., 1989, Methods for the collection and analysis of geothermal  
1118 and volcanic water and gas samples: New Zealand Department of Scientific and Industrial  
1119 Research, Chemistry Division Report 2387, 53 p

1120 Gurrieri, S., & Valenza, M. (1988) - Gas transport in natural porous mediums: A method for  
1121 measuring CO<sub>2</sub> flows from the ground in volcanic and geothermal areas. *Rend. Soc. Ital. Mineral.*  
1122 *Petrol.*, 43, 1151–1158

- 1123 Gurrieri, S., Liuzzo, M., and Giudice, G. (2008), Continuous monitoring of soil CO<sub>2</sub> flux on Mt. Etna:  
1124 The 2004–2005 eruption and the role of regional tectonics and volcano tectonics, *J. Geophys. Res.*,  
1125 113, B09206, doi:10.1029/2007JB005003, 2008
- 1126 Hajash, A., Armstrong, R.L. (1972) Paleomagnetic and radiometric evidence for the age of the  
1127 Comoros Islands, West Central Indian Ocean. *Earth Planet Sci Lett* 16:231–236
- 1128 Hesterberg, and Siegenthaler (1991) Production and stable isotopic composition of CO<sub>2</sub> in a soil  
1129 near Bern, Switzerland *Tellus*, 43B (1991), pp. 197-205
- 1130 Hoefs, J. (2015) Stable Isotope Geochemistry. Seventh Edition, 208 pp., *Springer International*  
1131 *Publishing Switzerland* 2015. ISBN 978-3-319-19715-9. DOI 10.1007/978-3-319-19716-6
- 1132 Horita, J. (2001) Carbon isotope exchange in the system CO<sub>2</sub>-CH<sub>4</sub> at elevated temperatures.  
1133 *Geochimica et Cosmochimica Acta*, Vol. 65, No. 12, pp. 1907–1919, 2001
- 1134 Hugoni, M., Escalas, A., Bernard, C., Nicolas, S., Jezequel, D., Vazzoler, F., et al. (2018).  
1135 Spatiotemporal variations in microbial diversity across the three domains of life in a tropical  
1136 thalassohaline lake (Dziani Dzaha, Mayotte Island). *Molecular ecology*, 27(23), 4775-4786.
- 1137 Hulston, J. R., and McCabe, W. J. (1962) Mass spectrometer measurements in the thermal areas of  
1138 New Zealand. Part 2. Carbon isotopic ratios. *Geochim. Cosmochim. Acta* 26, 399-410
- 1139 Irwin, W. P., and Barnes, I. (1980), Tectonic relations of carbon dioxide discharges and  
1140 earthquakes, *J. Geophys. Res.*, 85, 3115–3121, doi:10.1029/JB085iB06p03115
- 1141 Jovovic, I., Grossi, V., Adam, P., Cartigny, P., Antheaume, I., Sala, D., Milesi, V., Jezequel, D., Ader,  
1142 M., Gelin, F. (2017) Early diagenesis and preservation of sedimentary organic matter in an anoxic,  
1143 sulfidic lake (Lake Dziani Dzaha, Mayotte). 28<sup>th</sup> *International Meeting on organic geochemistry* 17-  
1144 22 September 2017, Florence, Italy
- 1145 Klimke, J., Franke, D., Gaedicke, C., Schreckenberger, B., Schnabel, M., Stollhofen, H., Rose, J. &  
1146 Chaheire, M., 2016. How to identify oceanic crust—Evidence for a complex break-up in the  
1147 Mozambique Channel, off East Africa, *Tectonophysics*, 693, 436-452
- 1148 Leboulanger, C., Agogue, H., Bernard, C., Bouvy, M., Carre, C., Cellamare, M., et al. (2017).  
1149 Microbial diversity and cyanobacterial production in Dziani Dzaha crater lake, a unique tropical  
1150 thalassohaline environment. *PLoS One*, 12(1), e0168879. Nehlig et al., 2013
- 1151 Lemoine, A., Briole, P., Bertil, D., Roullé, A., Foumelis, M., Thinon, I., Raucoules, D., et al. (2020)  
1152 The 2018–2019 seismo-volcanic crisis east of Mayotte, Comoros islands: seismicity and ground  
1153 deformation markers of an exceptional submarine eruption, *Geophysical Journal International*,  
1154 Volume 223, Issue 1, October 2020, Pages 22–44, <https://doi.org/10.1093/gji/ggaa273>
- 1155 Liuzzo, M., Di Muro, A., Giudice, G., Michon, L., Ferrazzini, V. and Gurrieri, S. (2015) New evidence  
1156 of CO<sub>2</sub> soil degassing anomalies on Piton de la Fournaise volcano and the link with volcano  
1157 tectonic structures. *Geochem. Geophys. Geosyst.* 16. <https://doi.org/10.1002/2015GC006032>

- 1158 Liuzzo, M., Gurrieri, S., Giudice, G. and Giuffrida, G. (2013) Ten years of soil CO<sub>2</sub> continuous  
1159 monitoring on Mt. Etna: exploring the relationship between processes of soil degassing and  
1160 volcanic activity. *Geochem. Geophys. Geosyst.* 14, 2886–2899
- 1161 Marty, B., Meynier, V., Nicolini, E., Griesshaber, E., and Toutain, J. P. (1993), Geochemistry of gas  
1162 emanations: A case study of the Reunion hot spot, Indian ocean, *Appl. Geochem.*, 8, 141–152
- 1163 Mazzini, A., Svensen, H., Etiope, E., Onderdonk, N., and Banks, D. (2011). Fluid origin, gas fluxes  
1164 and plumbing system in the sediment-hosted Salton Sea Geothermal System (California, USA). *J.*  
1165 *Volcanol. Geothermal Res.* 205, 67–83. doi: 10.1016/j.jvolgeores.2011.05.008
- 1166 Michon, L., 2016. The volcanism of the Comoros archipelago integrated at a regional scale. In:  
1167 Bachèlery, P., Lénat, J.-F., Di Muro, A., Michon, L. (Eds.), *Active Volcanoes of the Southwest Indian*  
1168 *Ocean: Piton de La Fournaise and Karthala.* Springer-Verlag, Berlin and Heidelberg, pp. 333–344
- 1169 Milesi, V. P., Debure, M., Marty, N. C. M., Capano, M, et al. (2020) Early Diagenesis of Lacustrine  
1170 Carbonates in Volcanic Settings: The Role of Magmatic CO<sub>2</sub> (Lake Dziani Dzaha, Mayotte, Indian  
1171 Ocean) *ACS Earth and Space Chemistry* 2020 4 (3), 363-378 DOI:  
1172 10.1021/acsearthspacechem.9b00279
- 1173 Milesi, V. P., Jézéquel, D., Debure, M., Cadeau, P., Guyot, F., Sarazin, G., Claret, F., Vennin, E.,  
1174 Chaduteau, C., Virgone, A., et al. (2019) Formation of Magnesium-Smectite during Lacustrine  
1175 Carbonates Early Diagenesis: Study Case of the Volcanic Crater Lake Dziani Dzaha (Mayotte- Indian  
1176 Ocean). *Sedimentology* 2019, 66, 983-1001
- 1177 Nehlig, P., Lacquement, F., Bernard, J., Audru, J., Caroff, M., Deparis, J., et al. (2013). Notice  
1178 explicative de la carte géologique Mayotte à 1/30.000 feuille Mayotte (1179). Orléans : BRGM, 74  
1179 p. Carte géologique par Lacquement F., Nehlig P., Bernard J. (2013).
- 1180 Nougier, J., Cantagrel, J.M., & Karche, J.P., 1986. The Comoros archipelago in the western Indian  
1181 Ocean: volcanology, geochronology and geodynamic setting, *Journal of African Earth Sciences* ,  
1182 5(2), 135-144
- 1183 Ono, A., Sano, Y., Wakita, H., Giggenbach, W. F. (1993) Carbon isotopes of methane and carbon  
1184 dioxide in hydrothermal gases of Japan, *Geochemical Journal*, Vol. 27, Issue 4-5, Pages 287-295  
1185 <https://doi.org/10.2343/geochemj.27.287>
- 1186 Ozima, M., and Podosek, F. A. (1983). *Noble Gas Geochemistry.* New York, NY: Cambridge  
1187 University Press
- 1188 Paonita, A., Caracausi, A., Martelli, M., & Rizzo, A. L. (2016) Temporal variations of helium isotopes  
1189 in volcanic gases quantify pre-eruptive refill and pressurization in magma reservoirs: The Mount  
1190 Etna case. *Geology* 44(7), 499–502
- 1191 Pelleter, A., Caroff, M., Cordier, C., Bachèlery, P., Nehlig, P., Debeuf, D., Arnaud, N., (2014) Melilite-  
1192 bearing lavas in Mayotte (France): an insight into the mantle source below the Comoros. *Lithos*  
1193 208–209, 281–297. <https://doi.org/10.1016/j.lithos.2014.09.012>

- 1194 Phethean, J.J.J. (2016) Madagascar's escape from Africa: a high-resolution plate reconstruction for  
1195 the Western Somali Basin and implications for supercontinent dispersal. *G-Cubed* 17, 5036–5055.  
1196 <https://doi.org/10.1002/2016GC006624>.Received
- 1197 Rabinowitz, P. D., Coffin, M. F., and Falvey, D. (1983) The separation of Madagascar and Africa,  
1198 *Science*, 220, 67–69
- 1199 Reid, R.C., Prausnitz, J.M., and Sherwood, T.K. (1977). The properties of gases and liquids. 3<sup>rd</sup> Ed.  
1200 *McGraw-Hill*
- 1201 REVOSIMA, 2019. Bulletin n°1 de l'activité sismo-volcanique à Mayotte, IPGP, Université de Paris,  
1202 OVPF, BRGM, Ifremer, CNRS, August, 23th, 2019,  
1203 [http://www.ipgp.fr/sites/default/files/ipgp\\_1er\\_bulletin\\_info\\_sismo\\_volcanique\\_mayotte-cor.pdf](http://www.ipgp.fr/sites/default/files/ipgp_1er_bulletin_info_sismo_volcanique_mayotte-cor.pdf)  
1204 and [www.ipgp.fr/revosima](http://www.ipgp.fr/revosima)
- 1205 Richet, P., Bottinga, Y., and Javoy, M. (1977) A review of hydrogen, carbon, nitrogen, oxygen,  
1206 sulfur, and chlorine stable isotope fractionation among gaseous molecules. *Ann. Rev. Earth Planet.*  
1207 *Sci.* 5, 65–110
- 1208 Rizzo, A.L., Caracausi, A., Chavagnac, V., Nomikou, P., Polymenakou, P.N., Mandalakis, M.,  
1209 Kotoulas G., Magoulas, A., Castillo, A., Lampridou, D., Maruszczak, N, and Sonke, J.E. (2019)  
1210 Geochemistry of CO<sub>2</sub>-Rich Gases Venting From Submarine Volcanism: The Case of Kolumbo  
1211 (Hellenic Volcanic Arc, Greece). *Front. Earth Sci.* 7:60. doi: 10.3389/feart.2019.00060
- 1212 Rizzo, A. L., Federico, C., Inguaggiato, S., Sollami, A., Tantillo, M., Vita, F., Bellomo, S., Longo, M.,  
1213 Grassa, F., and Liuzzo, M. (2015) The 2014 effusive eruption at Stromboli volcano (Italy):  
1214 Inferences from soil CO<sub>2</sub> flux and 3He/ 4He ratio in thermal waters, *Geophys. Res. Lett.*, 42, 2235–  
1215 2243, doi:10.1002/2014GL062955
- 1216 Rizzo, A. L., Caracausi, A., Chavagnac, V., Nomikou, P., Polymenakou, P. N., Mandalakis, M., et al.  
1217 (2016) Kolumbo submarine volcano (Greece): an active window into the Aegean subduction  
1218 system. *Sci. Rep.* 6:28013. doi: 10.1038/srep28013
- 1219 Roach, P., Milsom, J., Toland, C., Matchette-Downes, C., Budden, C., Riaroh, D., And Houmadi, N.  
1220 (2017) New evidence supports presence of continental crust beneath the Comoros: *Pesgb/Hgs*  
1221 *Africa Conference*. Aug 2017
- 1222 Rouff, A. A., Phillips, B. L., Cochiara, S. G., and Nagy, K. L. (2012) The Effect of dissolved humic acids  
1223 on aluminosilicate formation and associated carbon sequestration, *Appl. Environ. Soil Sci.*, 2012,  
1224 12, doi:10.1155/2012/430354
- 1225 Sanjuan, B., Baltassat, J., Bezelgues, S., Brach, M., Girard, J., & Mathieu, F. (2008). Estimation du  
1226 potentiel géothermique de Mayotte: Phase 2-Étape 2. Investigations géologiques, géochimiques et  
1227 géophysiques complémentaires, synthèse des résultats. Rapport BRGM/RP-56802-FR, 82 p., 18  
1228 fig., 3 tabl., 6 ann.
- 1229 Sano, Y., and Wakita, H. (1985) Distribution of 3He/4He ratios and its implications for geotectonic  
1230 structure of the Japanese Islands. *J. Geophys. Res.* 90, 8729-8741

- 1231 Sano, Y., and Marty, B. (1995). Origin of carbon in fumarolic gases from island arcs. *Chem. Geol.*  
1232 119, 265–274. doi: 10.1016/0009-2541(94)00097-R
- 1233 Sano, Y., Kagoshima, T., Takahata, N., et al. Ten-year helium anomaly prior to the 2014 Mt Ontake  
1234 eruption. *Sci Rep* 5, 13069 (2015). <https://doi.org/10.1038/srep13069>
- 1235 Schoell, M. (1980). The hydrogen and carbon isotopic composition of methane from natural gases  
1236 of various origins. *Geochim. Cosmochim. Acta* 44, 649–661. doi: 10.1016/0016-7037(80)90155-6
- 1237 Severinghaus, J.P., Bender, M.L., Keeling, R.F., Broecker, W.S. (1996) Fractionation of soil gases by  
1238 diffusion of water vapor, gravitational settling and thermal diffusion. *Geochim Cosmochim Acta*  
1239 60:1005–1018
- 1240 Späth, A., Roex, A. P. L., & Duncan, R. A. (1996). The Geochemistry of Lavas from the Gomoeres  
1241 Archipelago, Western Indian Ocean: Petrogenesis and Mantle Source Region Characteristics.  
1242 *Journal of Petrology*, 37(4), 961-991.
- 1243 Taran, Y. A., Kliger, G. A., Cienfuegos, E., and Shuykin, A. N. (2010). Carbon and hydrogen isotopic  
1244 compositions of products of open-system catalytic hydrogenation of CO<sub>2</sub>: implications for  
1245 abiogenic hydrocarbons in Earth's crust. *Geochim. Cosmochim. Acta* 74, 6112–6125. doi:  
1246 10.1016/j.gca.2010.08.012
- 1247 Traineau, H., Sanjuan, B., Brach, M., Audru, J-C. (2006) Etat des connaissances du potentiel  
1248 géothermique de Mayotte. Rapport final. BRGM/RP-54700-FR
- 1249 Tzevahirtzian, A., Zaragosi, S., Bachèlery, P., Biscara, L., & Marchès, E. (2021) Submarine  
1250 morphology of the Comoros volcanic archipelago. *Marine Geology*, 432, 106383.
- 1251 Welhan, J. A. (1988) Origins of methane in hydrothermal systems. *Chem. Geol.* 71, 183–198. doi:  
1252 10.1016/0009-2541(88)90114-3
- 1253 Zinke, J., Reijmer, J. J. G., & Thomassin, B. A. (2001) Seismic architecture and sediment distribution  
1254 within the Holocene barrier reef–lagoon complex of Mayotte (Comoro archipelago, SW Indian  
1255 Ocean). *Palaeogeography, Palaeoclimatology, Palaeoecology*, 175(1-4), 343-368.
- 1256

Table 2 – Soil CO<sub>2</sub> flux (g m<sup>-2</sup> d<sup>-1</sup>) surveys at Grande Comore and Mayotte

Grande Comore 2014		CO2 flux [g/(m <sup>2</sup> day)]
Latitude	Longitude	
1	11.760030 - 43.358620	0.00
2	11.760120 - 43.358940	992.60
3	11.760440 - 43.359140	0.00
4	11.760070 - 43.359300	0.00
5	11.760150 - 43.359830	5378.00
6	11.760410 - 43.360290	8.90
7	11.760550 - 43.361020	0.00
8	11.760560 - 43.361840	0.00
9	11.760500 - 43.362970	0.00
10	11.760040 - 43.363590	0.00
11	11.758290 - 43.362920	30.20
12	11.758200 - 43.362060	0.00
13	11.757630 - 43.361340	1242.70
14	11.758260 - 43.361440	5.70
15	11.758390 - 43.360850	24.50
16	11.758310 - 43.360750	153.50
17	11.758460 - 43.360220	7.90
18	11.758430 - 43.359810	0.00
19	11.758320 - 43.359130	21.30
20	11.758320 - 43.359790	6931.00
21	11.756940 - 43.356410	0.00
22	11.756960 - 43.357310	0.00
23	- - 43.358240	0.00

Grande Comore 2014		CO2 flux [g/(m <sup>2</sup> day)]
Latitude	Longitude	
24	11.756920 - 43.359290	4.00
25	11.757020 - 43.360120	1.30
26	11.756930 - 43.361020	4.60
27	11.756870 - 43.361130	9811.10
28	11.756960 - 43.361920	0.00
29	11.756930 - 43.362760	0.00
30	11.753250 - 43.364720	0.00
31	11.753290 - 43.363780	0.00
32	11.753240 - 43.362890	0.00
33	11.753270 - 43.361690	0.00
34	11.753660 - 43.360930	0.00
35	11.753490 - 43.359830	0.00
36	11.749920 - 43.361890	0.00
37	11.749930 - 43.361090	0.00
38	11.750010 - 43.360040	0.00
39	11.749950 - 43.359240	0.00
40	11.749550 - 43.358340	0.00
41	11.753260 - 43.355550	0.00
42	11.753240 - 43.359270	0.00
43	11.753320 - 43.358290	0.00
44	11.753340 - 43.357310	0.00
45	11.734620 - 43.356290	0.00

Grande Comore 2014		CO2 flux [g/(m <sup>2</sup> day)]
Latitude	Longitude	
46	11.731600 - 43.356970	0.00
47	11.728210 - 43.356650	2.50
48	11.727900 - 43.357430	2.60
49	11.728070 - 43.358410	1.10
50	11.727990 - 43.359880	1.50
51	11.728090 - 43.360430	1.40
52	11.728050 - 43.361270	1.90
53	11.727940 - 43.362010	4.70
54	11.728060 - 43.363120	9.10
55	11.728050 - 43.363840	3.60
56	11.727720 - 43.364480	3.80
57	11.732320 - 43.363310	21.50
58	11.732320 - 43.363260	796.70
59	11.732820 - 43.362400	0.00
60	11.731670 - 43.362060	10.10
61	11.731540 - 43.361200	6.10
62	11.731630 - 43.360350	3.30
63	11.731850 - 43.359590	7.20
64	11.731530 - 43.357740	4.10
65	11.735020 - 43.357890	5.30
66	11.735290 - 43.358390	8.10
67	11.735430 - 43.359460	4.90
68	- - 43.360180	8.00

Grande Comore 2014		CO2 flux [g/(m <sup>2</sup> day)]
Latitude	Longitude	
69	11.735350 - 43.361070	3.20
70	11.735510 - 43.362140	1.30
71	11.735580 - 43.362880	3.00
72	11.735400 - 43.361130	0.00
73	11.734460 - 43.361040	0.00
74	11.733640 - 43.360980	1.30
75	11.732860 - 43.360950	1.60
76	11.731890 - 43.360570	5.80
77	11.730180 - 43.359770	6.30
78	11.729260 - 43.359940	1.80
79	11.728800 - 43.360780	1.60
80	11.730240 - 43.360810	4.80
81	11.730710 - 43.361680	4.80
82	11.731120 - 43.362160	6.60
83	11.733480 - 43.362250	2.10
84	11.734470 - 43.362340	6.70
85	11.734260 - 43.363090	3.40
86	11.733520 - 43.363050	2.70
87	11.732700 - 43.363090	8.50
88	11.731730 - 43.363020	2.80
89	11.731340 - 43.363770	6.00
90	11.731630 - 43.364810	8.20

Grande Comore 2014		CO2 flux [g/(m <sup>2</sup> day)]
Latitude	Longitude	
91	11.732660 43.364940	6.10
92	11.733500 43.365130	7.50
93	11.734420 43.364980	1.30
94	11.735480 43.365060	2.90
95	11.735480 43.364010	5.40
96	11.734120 43.364140	313.40
97	11.733950 43.364120	8994.00
98	11.733710 43.364130	553.70
99	11.733580 43.364050	175.80
100	11.733390 43.363960	3046.10
101	11.732920 43.363410	17364.40
102	11.732400 43.363310	396.10
103	11.735470 43.365470	4.50
104	11.735410 43.366680	4.20
105	11.735290 43.367860	1.60
106	11.734920 43.368590	2.70
107	11.734950 43.369160	1.50
108	11.735100 43.370020	1.30
109	11.734880 43.371330	4.30
110	11.734890 43.372370	0.00
111	11.731630 43.372480	5.30
112	11.727760 43.371830	2.70
113	11.728050 43.370230	3.00
114	11.728340 43.369200	13.50
115	43.368350	1.30

Grande Comore 2014		CO2 flux [g/(m <sup>2</sup> day)]
Latitude	Longitude	
5	11.728570	
11	-	2.60
6	11.728670 43.367390	
11	-	5.70
7	11.728860 43.366670	
11	-	4.80
8	11.728690 43.365970	
11	-	4.40
9	11.728840 43.365040	
12	-	0.00
0	11.729510 43.365180	
12	-	9.00
1	11.730080 43.365400	
12	-	1.20
2	11.731050 43.365570	
12	-	5.50
3	11.731370 43.366580	
12	-	0.50
4	11.731860 43.367570	
12	-	4.00
5	11.731190 43.368440	
12	-	1.10
6	11.731050 43.369530	
12	-	3.00
7	11.731810 43.370240	
12	-	2.20
8	11.732570 43.370970	
12	-	4.40
9	11.738900 43.372030	
13	-	4.20
0	11.738920 43.371310	
13	-	1.60
1	11.738890 43.370270	1259
13	-	2.70
2	11.738950 43.369280	
13	-	1.50
3	11.738940 43.368460	
13	-	1.30
4	11.738900 43.367580	
13	-	4.20
5	11.738890 43.366800	
13	-	0.00
6	11.738880 43.365750	
13	-	2.50
7	11.738770 43.365270	
13	-	1.10
8	11.738960 43.363820	
13	-	1.50
9	11.738840 43.363260	

Grande Comore 2014		CO2 flux [g/(m <sup>2</sup> day)]
Latitude	Longitude	
14	-	1.40
0	11.739020 43.361900	
14	-	1.90
1	11.738830 43.361170	
14	-	4.60
2	11.738850 43.360300	
14	-	8.90
3	11.738890 43.359250	
14	-	3.60
4	11.738860 43.358360	
14	-	3.70
5	11.738570 43.357640	
14	-	21.10
6	11.738800 43.356490	
14	-	1.30
7	11.742410 43.360250	
14	-	2.20
8	11.742630 43.361150	
14	-	2.90
9	11.742560 43.362230	
15	-	7.20
0	11.742500 43.363040	
15	-	3.30
1	11.742550 43.363730	
15	-	6.00
2	11.742620 43.364710	
15	-	10.00
3	11.742450 43.365780	
15	-	0.00
4	11.742530 43.366600	
15	-	7.80
5	11.742480 43.367530	

Grande Comore 2017			CO2 flux [g/(m <sup>2</sup> day)]
Latitude	Longitude		
1	11.579000	43.311000	32.10
2	11.525000	43.337000	15.10
3	11.879000	43.407000	22.66
4	11.872000	43.399000	18.88
5	11.735000	43.329000	18.88
6	11.735000	43.329000	47.20
7	11.734000	43.328000	33.98
8	11.733000	43.327000	18.88
9	11.732000	43.326000	52.86
10	11.731000	43.326000	45.31
11	11.730000	43.324000	16.99
12	11.728000	43.323000	22.66
13	11.723000	43.250000	24.54
14	11.725000	43.249000	168.07
15	11.727000	43.250000	239.87
16	11.730000	43.250000	32.10
17	11.730000	43.249000	20.77
18	11.732000	43.250000	30.21
19	11.734000	43.249000	33.98
20	11.737000	43.250000	24.54
21	11.720000	43.249000	13.22
22	11.849000	43.332000	20.77
23	11.849000	43.330000	256.89
24	11.849000	43.328000	41.54
25	-	43.328000	98.18

Grande Comore 2017			CO2 flux [g/(m <sup>2</sup> day)]
Latitude	Longitude		
26	11.848000	43.321000	18.88
27	11.847000	43.316000	49.09
28	11.846000	43.314000	79.30
29	11.847000	43.311000	54.75
30	11.846000	43.306000	179.40
31	11.844000	43.303000	22.66
32	11.842000	43.301000	18.88
33	11.840000	43.299000	18.88
34	11.837000	43.297000	11.33
35	11.833000	43.292000	120.84
36	11.829000	43.288000	145.40
37	11.784000	43.271000	30.21
38	11.780000	43.267000	226.64
39	11.778000	43.265000	160.51
40	11.775000	43.264000	457.58
41	11.719000	43.249000	16.99
42	11.721000	43.245000	22.66
43	11.723000	43.245000	16.99
44	11.727000	43.244000	60.42
45	11.728000	43.243000	22.66
46	11.728000	43.240000	22.66
47	11.730000	43.242000	15.10
48	11.733000	43.241000	226.64
49	11.735000	43.240000	118.96

Grande Comore 2017			CO2 flux [g/(m <sup>2</sup> day)]
Latitude	Longitude		
50	11.737000	43.240000	94.41
51	11.740000	43.240000	43.42
52	11.742000	43.239000	16.99
53	11.747000	43.238000	22.66
54	11.748000	43.235000	50.98
55	11.752000	43.236000	52.86
56	11.759000	43.239000	11.33
57	11.759000	43.244000	37.76
58	11.560000	43.273000	9.44
59	11.566000	43.272000	94.41
60	11.570000	43.271000	13.221260
61	11.577000	43.269000	18.88
62	11.584000	43.267000	35.87
63	11.588000	43.266000	103.85
64	11.592000	43.266000	109.51
65	11.597000	43.263000	11.33
66	11.609000	43.263000	13.22
67	11.629000	43.307000	20.77
68	11.626000	43.309000	306.06
69	11.622000	43.312000	20.77
70	11.618000	43.314000	135.95
71	11.616000	43.315000	62.31
72	11.594000	43.378000	147.29
73	11.591000	43.382000	16.99
74	-	43.404000	98.18

Grande Comore 2017			CO2 flux [g/(m <sup>2</sup> day)]
Latitude	Longitude		
75	11.427000	43.399000	39.65
76	11.438000	43.399000	120.84
77	11.447000	43.402000	100.07
78	11.454000	43.402000	22.66
79	11.610000	43.365000	16.99
80	11.612000	43.363000	228.53
81	11.614000	43.357000	24.54
82	11.613000	43.350000	24.54
83	11.610000	43.346000	71.75
84	11.611000	43.341000	13.22

Grande Comore 2018			CO2 flux [g/(m <sup>2</sup> day)]
Latitude	Longitude		
1	11.876616	43.480066	7.55
2	11.878802	43.481346	7.55
3	11.879880	43.477517	13.22
4	11.879253	43.472302	7.55
5	11.882023	43.469274	13.22
6	11.885114	43.468817	9.44
7	11.884848	43.465353	11.33
8	11.885446	43.457200	7.55
9	11.886513	43.452216	18.88
10	11.888558	43.445997	28.32
11	-	43.442657	33.98

Grande Comore 2018		CO2 flux [g/(m <sup>2</sup> day)]
Latitude	Longitude	
11.890019	-	
12	11.890607 43.440029	22.66
13	11.893221 43.435186	20.77
14	11.894565 43.430336	28.32
15	11.756312 43.355270	7.55
16	11.758078 43.357018	9.44
17	11.757963 43.357585	7.55
18	11.757925 43.357977	9.44
19	11.758013 43.358559	9.44
20	11.757705 43.358812	7.55
21	11.757610 43.359170	16.99
22	11.757605 43.359566	30.21
23	11.757513 43.359916	22.66
24	11.757327 43.360275	11.33
25	11.757155 43.360631	802.29
26	11.757020 43.360974	951.98
27	11.756931 43.361213	45.31
28	11.756826 43.361449	283.36
29	11.756816 43.361700	32.10
30	11.756957 43.362062	9.44
31	11.757067 43.362450	7.55
32	11.757152 43.362882	7.55
33	11.732509 43.363215	15.10
34	11.637843 43.376308	11.33
35	11.636014 43.375007	22.66

Grande Comore 2018		CO2 flux [g/(m <sup>2</sup> day)]
Latitude	Longitude	
36	11.634025 43.373187	7.55
37	11.632313 43.371923	7.55
38	11.628818 43.372358	9.44
39	11.628904 43.372267	13.22
40	11.627732 43.368685	9.44
41	11.627151 43.365583	7.551261
42	11.622232 43.365063	5.66
43	11.619964 43.363529	5.66
44	11.615842 43.359638	47.20
45	11.614397 43.355913	7.55
46	11.613988 43.352644	7.55
47	11.613266 43.350659	16.99
48	11.611125 43.349181	30.21
49	11.609914 43.345950	11.33
50	11.612037 43.338725	28.32
51	11.613682 43.333515	9.44
52	11.614027 43.329282	7.55
53	11.614261 43.324552	9.44
54	11.614549 43.322405	20.77
55	11.614855 43.317845	20.77
56	11.615610 43.314634	16.99
57	11.618371 43.313629	28.32
58	11.621824 43.312271	9.44
59	11.626042 43.308930	105.74
60	- 43.309033	56.64

Grande Comore 2018		CO2 flux [g/(m <sup>2</sup> day)]
Latitude	Longitude	
11.625871	-	
61	11.626137 43.308888	120.84
62	11.780161 43.267323	67.97
63	11.770174 43.261717	11.33
64	11.759701 43.256409	37.76
65	11.758396 43.242995	84.96

Mayotte 2019		CO2 flux [g/(m <sup>2</sup> day)]
Latitude	Longitude	
1	45.286856 -12.799818	50.66
2	45.286886 -12.799780	3.50
3	45.286808 -12.799860	7.62
4	45.286780 -12.799913	4.02
5	45.286777 -12.799973	9.68
6	45.286748 -12.799982	5.70
7	45.286731 -12.800008	5.66
8	45.286717 -12.800075	3.90
9	45.286699 -12.800123	4.26
10	45.286686 -12.800178	3.95
11	45.286703 -12.800208	30.90
12	45.286661 -12.800261	2.92
13	45.286664 -12.800280	4.80
14	45.286682 -12.800339	2.04
15	45.286693 -12.800380	0.52
16	45.286672 -12.800439	1.64
17	45.286711 -12.800493	2.28
18	45.285713 -12.800167	5.28
19	45.285764 -12.800136	4.86
20	45.285806 -12.800110	12.65
21	45.285844 -12.800085	8.40
22	45.285883 -12.800070	17.57
23	45.285907 -12.800087	5.70
24	45.286072 -12.800006	22.82
25	45.286160 -12.800000	9.00
26	45.286118 -12.799945	17.06
27	45.286107 -12.799880	7.76
28	45.286142 -12.799805	5.36
29	45.286244 -12.799578	21.54

Mayotte 2019			CO2 flux [g/(m <sup>2</sup> day)]
Latitude	Longitude	Longitude	
30	45.286335	-12.799336	41.57
31	45.286491	-12.799352	14.70
32	45.286694	-12.799469	19.13
33	45.286883	-12.799525	6.48
34	45.287022	-12.799293	11.90
35	45.287079	-12.799116	8.10
36	45.287149	-12.798782	12.95
37	45.282678	-12.805537	0.45
38	45.282875	-12.805612	1.18
39	45.283069	-12.805955	0.00
40	45.282586	-12.805040	1.63
41	45.282379	-12.805167	1.00
42	45.277490	-12.802276	0.00
43	45.277386	-12.802210	0.00
44	45.277352	-12.802227	0.00
45	45.277246	-12.802167	4.45
46	45.277162	-12.802143	4.36
47	45.277292	-12.802176	1.21
48	45.277152	-12.802055	8.00
49	45.277126	-12.801957	1.64
50	45.277061	-12.801850	0.52
51	45.276823	-12.801281	15.70
52	45.276858	-12.801248	4.21
53	45.284543	-12.799820	11.56
54	45.284848	-12.799386	37.94
55	45.284923	-12.799228	173.44
56	45.285052	-12.799154	39.81
57	45.285033	-12.797719	0.00
58	45.285041	-12.797734	11.98
59	45.284897	-12.797933	4.84
60	45.284909	-12.798320	27.11
61	45.284959	-12.798641	13.28
62	45.284912	-12.798811	42.42
63	45.284776	-12.799008	9.62
64	45.285290	-12.797520	1.69
65	45.285442	-12.797118	2.12
66	45.285659	-12.796799	6.87
67	45.284645	-12.801006	2.36
68	45.284708	-12.800662	3.18
69	45.286793	-12.800945	3.26
70	45.288012	-12.799281	2.55
71	45.287850	-12.799243	0.49
72	45.287528	-12.799367	0.00
73	45.287306	-12.799543	4.04
74	45.287123	-12.799624	1.61

Mayotte 2019			CO2 flux [g/(m <sup>2</sup> day)]
Latitude	Longitude		
75	45.281475	-12.795606	1.99
76	45.281311	-12.796021	4.06
77	45.281218	-12.796457	6.18
78	45.281190	-12.797037	6.81
79	45.281312	-12.797480	2.53
80	45.281154	-12.798122	2.03
81	45.280780	-12.798222	7.22
82	45.281349	-12.797331	2.60
83	45.282582	-12.798498	5.60
84	45.282209	-12.799108	1.80
85	45.280079	-12.792672	1.06
86	45.279778	-12.793405	1.45
87	45.279577	-12.794203	3.39
88	45.279207	-12.795135	13.83
89	45.279342	-12.795964	0.00
90	45.278689	-12.796682	3.46
91	45.278386	-12.797120	2.67
92	45.278279	-12.797905	16.76
93	45.277967	-12.798124	0.00
94	45.277448	-12.798648	7.81
95	45.255220	-12.782986	1.97
96	45.255288	-12.781948	3.81
97	45.254958	-12.781035	0.00
98	45.257887	-12.783449	2.11
99	45.260400	-12.785424	3.47
100	45.261339	-12.786133	2.61
101	45.262178	-12.786088	0.00
102	45.261778	-12.785416	3.32
103	45.264903	-12.787605	5.05
104	45.268356	-12.789905	5.71
105	45.268894	-12.791590	2.73
106	45.273430	-12.794984	8.00
107	45.274379	-12.794448	5.34
108	45.275029	-12.794076	1.03
109	45.275483	-12.793842	2.43
110	45.275939	-12.793916	7.21

Mayotte 2019			CO2 flux [g/(m <sup>2</sup> day)]
Latitude	Longitude		
111	45.276297	-12.793910	12.45
112	45.276781	-12.793827	3.11
113	45.277189	-12.793428	2.68
114	45.277539	-12.792994	1.97
115	45.278188	-12.792446	5.57
116	45.280727	-12.766360	0.00
117	45.280762	-12.768051	0.39
118	45.279645	-12.770106	2.52
119	45.279858	-12.771997	3.38
120	45.280814	-12.774220	2.93
121	45.281827	-12.776119	1.50
122	45.294567	-12.783769	1.70
123	45.293457	-12.784258	6.53
124	45.292021	-12.784650	3.35
125	45.290841	-12.785500	26.03
126	45.289486	-12.785186	6.06
127	45.288814	-12.784143	10.06
128	45.288652	-12.783974	11.54
129	45.289141	-12.783073	6.76
130	45.288129	-12.782416	1.27
131	45.286670	-12.781859	4.26
132	45.285204	-12.782200	0.00
133	45.283348	-12.782728	6.09
Mayotte Bubbling Area Sea 2019			CO2 flux

Mayotte 2019			CO2 flux [g/(m <sup>2</sup> day)]
Latitude	Longitude		
134	45.288840	-12.800657	40
135	45.288840	-12.800657	40
136	45.288818	-12.800576	64
137	45.288818	-12.800576	64
138	45.288787	-12.800533	38
139	45.288787	-12.800533	38
140	45.288766	-12.800518	59
141	45.288766	-12.800518	59
142	45.288766	-12.800518	59
143	45.288766	-12.800518	59
144	45.288734	-12.800502	13
145	45.288734	-12.800502	13
146	45.288676	-12.800483	99
147	45.288611	-12.800534	64
148	45.288257	-12.799866	93
149	45.288257	-12.799866	93
150	45.288257	-12.799866	93
151	45.288257	-12.799866	93
152	45.288257	-12.799866	93
153	45.288257	-12.799866	93
154	45.288257	-12.799866	93
155	45.288257	-12.799866	93
156	45.288257	-12.799866	93
157	45.288257	-12.799866	93
158	45.288257	-12.799866	93
159	45.288257	-12.799866	93
160	45.288257	-12.799866	93
161	45.288257	-12.799866	93
162	45.288257	-12.799866	93
163	45.288257	-12.799866	93
164	45.288257	-12.799866	93
165	45.288257	-12.799866	93
166	45.288257	-12.799866	93
167	45.288257	-12.799866	93
168	45.288257	-12.799866	93
169	45.288257	-12.799866	93
170	45.288257	-12.799866	93
171	45.288257	-12.799866	93
172	45.288257	-12.799866	93
173	45.288257	-12.799866	93
174	45.288257	-12.799866	93
175	45.288257	-12.799866	93
176	45.288257	-12.799866	93
177	45.288257	-12.799866	93
178	45.288257	-12.799866	93
179	45.288257	-12.799866	93
180	45.288257	-12.799866	93
181	45.288257	-12.799866	93
182	45.288257	-12.799866	93
183	45.288257	-12.799866	93
184	45.288257	-12.799866	93
185	45.288257	-12.799866	93
186	45.288257	-12.799866	93
187	45.288257	-12.799866	93
188	45.288257	-12.799866	93
189	45.288257	-12.799866	93
190	45.288257	-12.799866	93
191	45.288257	-12.799866	93
192	45.288257	-12.799866	93
193	45.288257	-12.799866	93
194	45.288257	-12.799866	93
195	45.288257	-12.799866	93
196	45.288257	-12.799866	93
197	45.288257	-12.799866	93
198	45.288257	-12.799866	93
199	45.288257	-12.799866	93
200	45.288257	-12.799866	93

Mayotte 2019			CO2 flux [g/(m <sup>2</sup> day)]
Latitude	Longitude		
201	45.288257	-12.799866	93
202	45.288257	-12.799866	93
203	45.288257	-12.799866	93
204	45.288257	-12.799866	93
205	45.288257	-12.799866	93
206	45.288257	-12.799866	93
207	45.288257	-12.799866	93
208	45.288257	-12.799866	93
209	45.288257	-12.799866	93
210	45.288257	-12.799866	93
211	45.288257	-12.799866	93
212	45.288257	-12.799866	93
213	45.288257	-12.799866	93
214	45.288257	-12.799866	93
215	45.288257	-12.799866	93
216	45.288257	-12.799866	93
217	45.288257	-12.799866	93
218	45.288257	-12.799866	93
219	45.288257	-12.799866	93
220	45.288257	-12.799866	93
221	45.288257	-12.799866	93
222	45.288257	-12.799866	93
223	45.288257	-12.799866	93
224	45.288257	-12.799866	93
225	45.288257	-12.799866	93
226	45.288257	-12.799866	93
227	45.288257	-12.799866	93
228	45.288257	-12.799866	93
229	45.288257	-12.799866	93
230	45.288257	-12.799866	93
231	45.288257	-12.799866	93
232	45.288257	-12.799866	93
233	45.288257	-12.799866	93
234	45.288257	-12.799866	93
235	45.288257	-12.799866	93
236	45.288257	-12.799866	93
237	45.288257	-12.799866	93
238	45.288257	-12.799866	93
239	45.288257	-12.799866	93
240	45.288257	-12.799866	93
241	45.288257	-12.799866	93
242	45.288257	-12.799866	93
243	45.288257	-12.799866	93
244	45.288257	-12.799866	93
245	45.288257	-12.799866	93
246	45.288257	-12.799866	93
247	45.288257	-12.799866	93
248	45.288257	-12.799866	93
249	45.288257	-12.799866	93
250	45.288257	-12.799866	93
251	45.288257	-12.799866	93
252	45.288257	-12.799866	93
253	45.288257	-12.799866	93
254	45.288257	-12.799866	93
255	45.288257	-12.799866	93
256	45.288257	-12.799866	93
257	45.288257	-12.799866	93
258	45.288257	-12.799866	93
259	45.288257	-12.799866	93
260	45.288257	-12.799866	93
261	45.288257	-12.799866	93
262	45.288257	-12.799866	93
263	45.288257	-12.799866	93
264	45.288257	-12.799866	93
265	45.288257	-12.799866	93
266	45.288257	-12.799866	93
267	45.288257	-12.799866	93
268	45.288257	-12.799866	93
269	45.288257	-12.799866	93
270	45.288257	-12.799866	93
271	45.288257	-12.799866	93
272	45.288257	-12.799866	93
273	45.288257	-12.799866	93
274	45.288257	-12.799866	93
275	45.288257	-12.799866	93
276	45.288257	-12.799866	93
277	45.288257	-12.799866	93
278	45.288257	-12.799866	93
279	45.288257	-12.799866	93
280	45.288257	-12.799866	93
281	45.288257	-12.799866	93
282	45.288257	-12.799866	93
283	45.288257	-12.799866	93
284	45.288257	-12.799866	93
285	45.288257	-12.799866	93
286	45.288257	-12.799866	93
287	45.288257	-12.799866	93
288	45.288257	-12.799866	93
289	45.288257	-12.799866	93
290	45.288257	-12.799866	93
291	45.288257	-12.799866	93
292	45.288257	-12.799866	93
293	45.288257	-12.799866	93
294	45.288257	-12.799866	93
295	45.288257	-12.799866	93
296	45.288257	-12.799866	93
297	45.288257	-12.799866	93
298	45.288257	-12.799866	93
299	45.288257	-12.799866	93
300	45.288257	-12.799866	93
301	45.288257	-12.799866	93
302	45.288257	-12.799866	93
303	45.288257	-12.799866	93
304	45.288257	-12.799866	93
305	45.288257	-12.799866	93
306	45.288257	-12.799866	93
307	45.288257	-12.799866	93
308	45.288257	-12.799866	93
309	45.288257	-12.799866	93
310	45.288257	-12.799866	93
311	45.288257	-12.799866	93
312	45.288257	-12.799866	93
313	45.288257	-12.799866	93
314	45.288257	-12.799866	93
315	45.288257	-12.799866	93
316	45.288257	-12.799866	93
317	45.288257	-12.799866	93
318	45.288257	-12.799866	93
319	45		

Mayotte 2019			CO2 flux [g/(m <sup>2</sup> day)]
Latitude	Longitude		
			94
50	45.289290	-12.800481	8730.5 8
51	45.289524	-12.800485	5952.6 7
52	45.289584	-12.800270	15537. 98
53	45.289039	-12.800000	14289. 19

1262

1263

Mayotte 2020			CO2 flux [g/(m <sup>2</sup> day)]
	Latitude	Longitude	
1	45.28444	-12.7644	4.81
2	45.28326	-12.7654	6.69
3	45.28096	-12.7656	5.95
4	45.28058	-12.7681	15.93
5	45.27964	-12.7702	34.82
6	45.27978	-12.7718	17.22
7	45.28066	-12.7736	26.00
8	45.28116	-12.7753	17.04
9	45.28222	-12.7771	13.72
10	45.28137	-12.7787	16.14
11	45.28062	-12.7801	15.93
12	45.27904	-12.7812	29.44
13	45.27759	-12.7818	39.00
14	45.27644	-12.7828	8.52
15	45.27516	-12.7842	4.78
16	45.27395	-12.7852	48.00
17	45.27289	-12.7863	8.96
18	45.26905	-12.7873	10.93
19	45.26936	-12.7895	19.95
20	45.26946	-12.7896	3.85
21	45.26819	-12.789	7.94
22	45.2847	-12.7824	62.91
23	45.28392	-12.7826	159.30
24	45.28293	-12.7828	28.73
25	45.28168	-12.783	6.07
26	45.28016	-12.7838	48.72
27	45.27952	-12.7842	14.55
28	45.27929	-12.7856	13.95
29	45.2793	-12.7856	37.36
30	45.27905	-12.7868	4.03
31	45.27994	-12.7891	15.85
32	45.28001	-12.7911	12.56
33	45.28612	-12.7999	29.08

1264

1265

1266

1267 Table 3 – Synopsis of soil CO<sub>2</sub> results and relative method used and year of measurements

CO <sub>2</sub> flux [g m <sup>-2</sup> day <sup>-1</sup> ]	Grande Comore		Grande Comore		Mayotte		Mayotte Bubbling Sea
	2014		2017	2018	2019	2020	2019
<b>Min</b>	0.0		9.44	5.66	0.0	3.85	12.2
<b>Max</b>	17364.4		457.58	951.98	173.4	159.3	70485.7
<b>Average</b>	365.6		67.61	51.91	8.2	23.90	21084.0
<b>σ</b>	1886.3		79.41	153.91	17.0	28.39	12045.2
	<i>Accumulation Chamber</i>		<i>Dynamic Concentration (K=30)</i>		<i>Accumulation Chamber</i>		<i>Accumulation Chamber</i>

1268

1269

1270

1271